Collinear artificial equilibrium point maintenance with a wrinkled solar sail

Christian Bianchi, Lorenzo Niccolai*, Giovanni Mengali, Alessandro A. Quarta

Dipartimento di Ingegneria Civile e Industriale, University of Pisa, Italy

Abstract

Propellantless propulsion systems allow innovative mission scenarios to be envisaged, including the generation and the stabilization of artificial equilibrium points in the circular restricted three-body problem. This paper discusses the generation of collinear, L_1-type, artificial equilibrium points in the Sun-[Earth+Moon] system, using a (photonic) solar sail. The main contribution of this paper is to investigate the spacecraft dynamics and its control when the sail propulsive acceleration is described with a recent thrust model that accounts for the presence of wrinkles on the membrane surface. In particular, an H_∞ static output-feedback control based on reflectivity control devices is proposed to stabilize the spacecraft around the L_1-type artificial equilibrium point, and a procedure is described for estimating the required area covered by those devices as a fraction of the whole solar sail surface.

Keywords: wrinkled solar sail, artificial equilibrium point, reflectivity control devices, H_∞ static output-feedback control

Nomenclature

A	=	sail reflective area, $[\mathrm{m}^2]$
$\{\mathbb{A}, \mathbb{B}, \mathbb{B}_v, \mathbb{C}, \mathbb{D}, \mathbb{L}, \mathbb{P}, \mathbb{S}\}$	=	auxiliary matrices
$\boldsymbol{a}$	=	dimensionless propulsive acceleration vector
B	=	non-Lambertian coefficient
$\{b_1, b_2, b_3\}$	=	dimensionless force coefficients, see Eqs. (6)
C	=	Sun-[Earth+Moon]'s center of mass
$\{c_1, c_2, c_3\}$	=	dimensionless constants, see Eqs. (24)–(26)
$\boldsymbol{d}$	=	disturbance vector
G	=	universal gravitational constant, $[\mathrm{N\,m^2/kg^2}]$
H	=	spacecraft main body height, [m]
$\{I_1, I_2, I_3\}$	=	spacecraft principal moment of inertia, $[\mathrm{kg\,m^2}]$
$\mathbb{I}$	=	identity matrix
$\mathbb{K} \triangleq [\mathbb{K}_p \, \mathbb{K}_d]$	=	control gain matrix
k	=	relative area variation, see Eq. (69)
$\{k_{pi}, k_{di}\}$	=	proportional and derivative gains ($i = 1, \ldots 3$)
$\boldsymbol{L}$	=	control torque level arm vector (with $L \triangleq \|\boldsymbol{L}\|$), [m]
l	=	Sun-[Earth+Moon] distance, [au]
$\boldsymbol{M}$	=	control torque vector, $[\mathrm{N\,m}]$

*Corresponding author

Email addresses: christian.bianchi@phd.unipi.it (Christian Bianchi), lorenzo.niccolai@ing.unipi.it (Lorenzo Niccolai), g.mengali@ing.unipi.it (Giovanni Mengali), a.quarta@ing.unipi.it (Alessandro A. Quarta)

Published in Aerospace Science and Technology, Vol. 119, December 2021, pp. 107150 (1–14). doi: https://doi.org/10.1016/j.ast.2021.107150

M = primary's mass, [kg]
m = spacecraft total mass, [kg]
m_{PL} = payload mass, [kg]
N_{TEC} = number of TECs
$\hat{\boldsymbol{n}}$ = normal unit vector
$\mathbb{O}$ = zero matrix
$\{\mathbb{Q}, \mathbb{R}\}$ = weighting matrices
$P_{\oplus}$ = solar radiation pressure at 1 au, [N/m^2]
R = spacecraft main body radius, [m]
$\mathbb{R}_{\mathcal{T}_1}^{\mathcal{T}_2}$ = rotational matrix from $\mathcal{T}_1$ to $\mathcal{T}_2$
$\boldsymbol{r}_{\odot}$ = dimensionless Sun-spacecraft vector (with $r_{\odot} \triangleq \|\boldsymbol{r}_{\odot}\|$)
S = spacecraft center of mass
$\boldsymbol{T}$ = solar sail thrust vector, [N]
t = time, [s]
$\{\mathcal{T}_B, \widetilde{\mathcal{T}}_B\}$ = body-fixed reference frames
$\mathcal{T}_S$ = synodic reference frame
$\mathcal{T}_{SBF}$ = sail boom frame
$\boldsymbol{u}$ = control vector
$\boldsymbol{x}$ = state vector
$\boldsymbol{y}$ = vector of measured state variables
$\{\alpha, \psi\}$ = Euler angles, [deg]
β = sail lightness number
δA = reflective area reduction, [m^2]
γ = attenuation factor, see Eq. (49)
$\delta\beta$ = sail lightness number variation
$\delta\boldsymbol{r}$ = dimensionless position perturbation
$\delta\dot{\boldsymbol{r}}$ = dimensionless velocity perturbation
ϵ = emissivity coefficient
η = sail/RCD efficiency
Θ = angle between $\hat{\boldsymbol{n}}_0$ and $\hat{\tilde{\boldsymbol{n}}}$, [deg]
θ = cone angle, [deg]
κ = absorbtion coefficient
Λ_i = i-th eigenvalue of matrix $\mathbb{A}$
λ = auxiliary constant, see Eq. (93)
μ = [Earth+Moon]'s dimensionless mass
ρ_d = diffuse reflection coefficient
ρ_s = specular reflection coefficient
$\widetilde{\phi}$ = auxiliary angle, [deg]
σ = solar sail loading, [g/m^2]
$\sigma_{\rm cr}$ = critical sail loading, [g/m^2]

Subscripts

$\odot$ = relative to the Sun
$\oplus$ = relative to the [Earth+Moon]
0 = related to unwrinkled sail
1 = related to β-control RCDs
2 = related to attitude control RCDs
b = sail back-side
f = sail front-side
e = AEP nominal value
j = generic TEC
off = RCD off-state
on = RCD on-state

RCD = relative to RCDs
s = related to the sail reflective membrane

Superscripts

$\cdot$ = derivative w.r.t. dimensionless time
$\sim$ = relative to a wrinkled sail
$\wedge$ = unit vector

1. Introduction

A solar sail is a propulsive system that exploits the solar radiation pressure acting on a thin reflective membrane (or some spinning blades) to generate thrust without any propellant consumption [1, 2, 3]. Due to their peculiar working principle, propellantless propulsive systems like solar sails may be used in mission scenarios otherwise difficult or even impossible to accomplish with conventional (i.e., chemical or electric) thrusters, including the generation and maintenance of non-Keplerian orbits [4, 5, 6, 7, 8], the exploration of near-Earth asteroids [9, 10] and of the inner Solar System [11, 12, 13, 14], the transfer to and maintenance at an heliostationary position [15, 16, 17], and the exploration of outer Solar System [18, 19, 20, 21]. The interest of the scientific community on solar sailing has led to the design of some solar sail-based missions, including the recent JAXA's IKAROS [22], NASA's NanoSail-D2 [23] and Planetary Society's LightSail [24], and the plan or proposal of new missions such as OKEANOS [25], NEA Scout [26, 27, 28] and Solar Cruiser [29]; see Fig. 1.

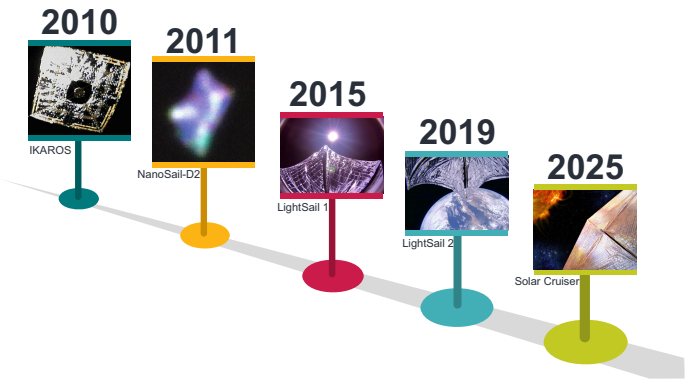

Figure 1: Timeline of the main past and planned solar sail-based missions.

Among all possible solar sail-based mission scenarios, this work deals with the generation of an artificial equilibrium point (AEP) in the Sun-[Earth+Moon] circular restricted three-body problem (CRTBP) [30, 31, 32]. In particular, the Sun-[Earth+Moon] CRTBP assumes that the only relevant gravitational forces acting on the spacecraft are those generated by the Sun's mass and the total mass of the Earth and the Moon, the latter being concentrated in a single point, placed at a distance of 1 au from the Sun, which revolves around the star on the Ecliptic plane with a period equal to 1 year. An AEP is generated when the propulsive acceleration continuously balances the centrifugal, Coriolis, and gravitational accelerations. Several types of AEPs [33, 34, 35] may be generated by a solar sail in a CRTBP framework, but we concentrate on an L_1-type AEP, which could be exploited by a solar observation spacecraft to provide an early warning in case of solar flares, geomagnetic storms, or other catastrophic solar events. Currently, NASA's satellite Advanced Composition Explorer (ACE) is tracking a periodic orbit in the vicinity of the natural Sun-[Earth+Moon] L_1 point. This guarantees a warning time of about 1 hour, under the assumption of an average solar wind velocity of about 400 km/s [36]. A spacecraft equipped with a propellantless propulsive system is able to generate an AEP closer to the Sun than the natural L_1 point, thus increasing the warning time. A major problem is that L_1-type AEPs are known to be unstable, so that a control system is necessary to stabilize

the spacecraft dynamics. In this paper, we discuss a control system based on the use of reflectivity control devices (RCDs), which are actuators capable of modifying their optical properties under the application of a suitable load voltage. In principle, RCDs may be used to generate control torques and also to vary the sail propulsive acceleration magnitude. Their application for controlling the attitude of a solar sail in deep space has been successfully tested in JAXA's IKAROS mission [37, 38].

The problem of generation and stabilization of an L_1-type AEP by means of a propellantless propulsive system has been discussed by several authors [33, 39, 40, 41, 42]. The main contribution of this paper may be summarized in the following points. Firstly, our analysis concentrates on a solar sail-based L_1-type AEP maintenance, but, unlike other works available in the literature, the propulsive acceleration generated by the sail is here estimated with a recent thrust model that accounts for the actual sail membrane optical properties and the presence of wrinkles as film deformations [43, 44]. Moreover, an innovative H_∞ static output-feedback control law, discussed in Ref. [45], is applied to the wrinkled solar sail-case, and its effectiveness is illustrated in a potential mission scenario. Finally, a procedure is proposed to obtain a first estimate of the total sail area and to quantify the fraction of area covered by RCDs.

The rest of the paper is organized as follows. Section 2 discusses the nominal (equilibrium) requirements for an L_1-type AEP maintenance with a wrinkled sail, whose thrust model is detailed in the Appendix. Section 3 describes the H_∞ static output-feedback control that is used to stabilize the perturbed dynamics in the vicinity of the target AEP. Section 3 also provides the mathematical tools necessary to calculate the required control torques, and discusses a preliminary sail design procedure. Then, Section 4 simulates the proposed control law in a test case scenario. Finally, the Conclusion section summarizes the main outcomes of this work.

2. Mathematical preliminaries and mission description

Consider the problem of generation and maintenance of a collinear AEP in the Sun-[Earth+Moon] CRTBP, where the Sun's mass is $M_\odot$ while the [Earth+Moon]'s mass is $M_\oplus$. We concentrate on an L_1-type AEP, so that the solar sail-based spacecraft is placed between the Sun and the natural L_1 Lagrange point, the position of which is along the Sun-Earth line at a distance of about 0.01 au from Earth toward the Sun. In case of catastrophic solar events, such as solar flares or coronal mass ejections, a spacecraft placed at such an L_1-type AEP could send a signal to a station on Earth with a warning time that varies depending on the actual Earth-spacecraft distance.

Using the standard notation of the CRTBP, consider a right-handed (synodic) reference frame $\mathcal{T}_S(C; \hat{\boldsymbol{\imath}}, \hat{\boldsymbol{\jmath}}, \hat{\boldsymbol{k}})$ with its origin C coinciding with the Sun-[Earth+Moon] center of mass, the unit vector $\hat{\boldsymbol{\imath}}$ pointing from C to [Earth+Moon] center of mass, and the unit vector $\hat{\boldsymbol{k}}$ being aligned with the [Earth+Moon] angular momentum vector; see Fig. 2.

The spacecraft dynamics in $\mathcal{T}_S$ is described, considering gravitational, centrifugal, Coriolis, and propulsive accelerations, by the second order vectorial differential equation [30, 33]

$$\ddot{\boldsymbol{r}}_\odot + 2\,\hat{\boldsymbol{k}} \times \dot{\boldsymbol{r}}_\odot + \hat{\boldsymbol{k}} \times \left[\hat{\boldsymbol{k}} \times \left(\boldsymbol{r}_\odot - \mu\,\hat{\boldsymbol{\imath}}\right)\right] + \frac{1-\mu}{r_\odot^3}\boldsymbol{r}_\odot + \frac{\mu}{\left\|\boldsymbol{r}_\odot - \hat{\boldsymbol{\imath}}\right\|^3}\left(\boldsymbol{r}_\odot - \hat{\boldsymbol{\imath}}\right) = \boldsymbol{a} \tag{1}$$

where $\mu \triangleq M_\oplus/(M_\odot + M_\oplus) \simeq 3.036 \times 10^{-6}$ is the [Earth+Moon] dimensionless mass, $\boldsymbol{r}_\odot$ is the dimensionless Sun-spacecraft vector (with $r_\odot \triangleq \|\boldsymbol{r}_\odot\|$), and $\boldsymbol{a}$ is the dimensionless sail propulsive acceleration vector. In Eq. (1), the Sun-[Earth+Moon] nominal distance ($l \triangleq 1$ au) and the total mass of the primaries ($M_\odot + M_\oplus$) are taken as the reference length and mass, respectively, while the time unit is chosen to make unitary the angular velocity of the primaries $\omega_\oplus \simeq 1.9965 \times 10^{-7}$ rad/s. Finally, the dot symbol denotes a derivative taken with respect to $t\,\omega_\oplus$, where t is the time.

To complete the system dynamics, the sail propulsive acceleration vector must be expressed with a suitable thrust model. Usually, the thrust vector is written as a function of the reflective area A and of the solar sail attitude, defined by the orientation of the unit vector $\hat{\boldsymbol{n}}$ normal to the sail nominal plane in the direction opposite to the Sun. In this context, several thrust models have been discussed in literature, including the ideal sail [46, 47], the optical sail [46, 47] with degradation [48, 49], or even more complex models [50, 51, 52, 53]. In this paper, a realistic thrust model is considered, which takes into account the presence of wrinkles on the reflective surface and models their effect on the magnitude and direction of

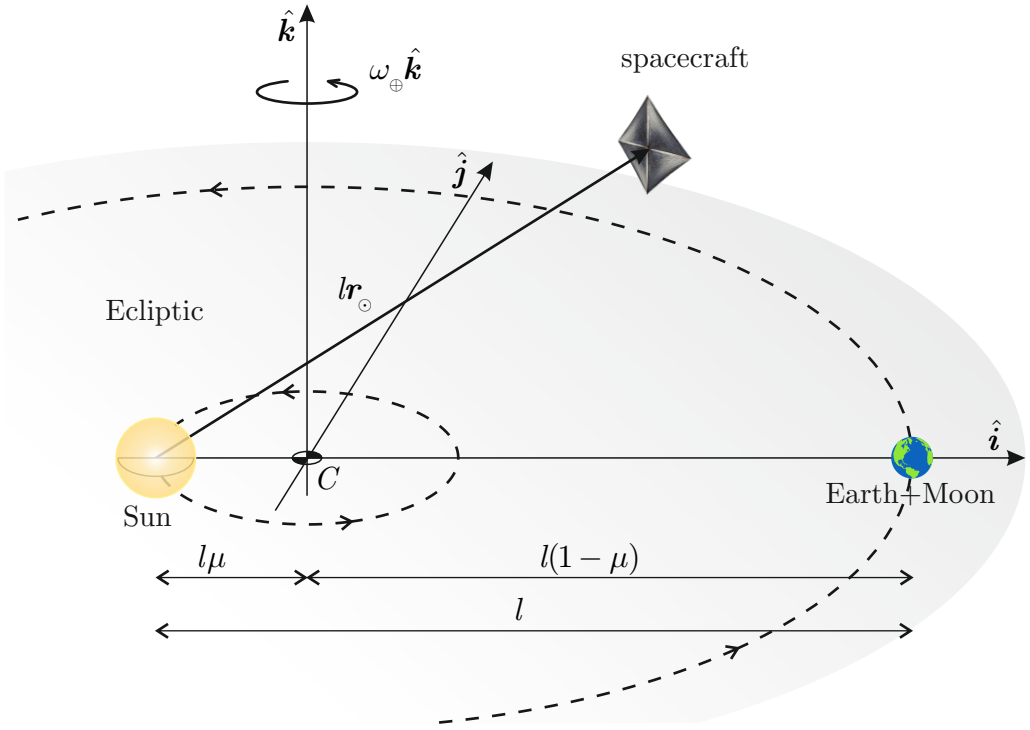

Figure 2: Sketch of the synodic frame $\mathcal{T}_S$ with CRTBP notation.

the sail thrust vector. In fact, wrinkles modify the thrust direction and affect the propulsive acceleration magnitude by reducing the effective sail area of a quantity $\delta A < 0$ [43, 44]. The overall effect on the thrust vector direction is modelled by defining a unit vector $\widetilde{\hat{\boldsymbol{n}}}$ normal to the unwrinkled-sail nominal plane.

According to the mathematical model thoroughly discussed in Refs. [43, 44], and bearing in mind the scheme of Fig. 2, the dimensionless sail propulsive acceleration vector $\boldsymbol{a}$ may be expressed as

$$\boldsymbol{a} = \frac{P_{\oplus}\, A/m}{G\,(M_{\odot}+M_{\oplus})/l^2}\left(1+\frac{\delta A}{A}\right)\left(\frac{1}{r_{\odot}}\right)^2 \cos\widetilde{\theta}\Big[\left(2\,\rho_s\,\cos\widetilde{\theta}+\rho_d\,B_f\right)\widetilde{\hat{\boldsymbol{n}}}+\left(\kappa+\rho_d\right)\hat{\boldsymbol{r}}_{\odot}\Big] \tag{2}$$

where G is the universal gravitational constant, $P_{\oplus} \triangleq 4.56\times10^{-6}\,\mathrm{N/m^2}$ is the solar radiation pressure at the reference distance l, m is the constant spacecraft mass, ρ_s is the sail film specular reflection coefficient, ρ_d is the sail film diffuse reflection coefficient, κ is the sail film absorption coefficient, B_f is the non-Lambertian coefficient of the sail front side, and $\hat{\boldsymbol{r}}_{\odot} \triangleq \boldsymbol{r}_{\odot}/r_{\odot}$ is the Sun-spacecraft unit vector. In Eq. (2), the term $\widetilde{\theta} \in [0, \pi/2]$ rad is the wrinkled-sail cone angle, defined as the angle between the directions of $\hat{\boldsymbol{r}}_{\odot}$ and $\widetilde{\hat{\boldsymbol{n}}}$, viz.

$$\widetilde{\theta} \triangleq \arccos\left(\widetilde{\hat{\boldsymbol{n}}}\cdot\hat{\boldsymbol{r}}_{\odot}\right) \tag{3}$$

Note that Eq. (2) accounts for the effect of wrinkles affecting both the propulsive acceleration vector magnitude and its direction. More details on the derivation of Eq. (2) may be found in the Appendix.

The dimensionless propulsive acceleration vector can be rewritten in a more compact form as

$$\boldsymbol{a} = \widetilde{\beta}\left(\frac{1-\mu}{r_{\odot}^2}\right)\left(\frac{\cos\widetilde{\theta}}{b_1+b_2+b_3}\right)\left[b_1\,\hat{\boldsymbol{r}}_{\odot}+\left(b_2\,\cos\widetilde{\theta}+b_3\right)\widetilde{\hat{\boldsymbol{n}}}\right] \tag{4}$$

where $\widetilde{\beta}$ is the wrinkled-sail lightness number, defined as the (dimensionless) ratio of the maximum propulsive acceleration magnitude (when $\widetilde{\theta}=0$, that is, in a Sun-facing condition [54]) to the local Sun's gravitational acceleration, viz.

$$\widetilde{\beta} \triangleq \frac{P_{\oplus}\,A}{m}\left(1+\frac{\delta A}{A}\right)\frac{l^2}{G\,M_{\odot}}\left(b_1+b_2+b_3\right) \tag{5}$$

In Eqs. (4)-(5), the terms $\{b_1,\, b_2,\, b_3\}$ are the sail force coefficients [55, 56] defined as

$$b_1 = \kappa + \rho_d \tag{6}$$

$$b_2 = 2\,\rho_s \tag{7}$$

$$b_3 = B_f\,\rho_d \tag{8}$$

According to the most recent measurements of the solar sail optical properties [57, 58], the values of the optical parameters of a typical solar sail membrane, composed of a polymeric substrate (made of CP1, Kapton, or Mylar) and an aluminum front surface coating, are

$$\rho_s = 0.8099 \quad , \quad \rho_d = 0.1001 \quad , \quad \kappa = 0.0900 \quad , \quad B_f = 0.79 \tag{9}$$

so that the value of the force coefficients are

$$b_1 \simeq 0.1901 \quad , \quad b_2 \simeq 1.6198 \quad , \quad b_3 \simeq 0.0791 \tag{10}$$

An L_1-type AEP at a dimensionless distance $r_{\odot_e}$ from the Sun is obtained by enforcing, in Eq. (1), the conditions

$$\dot{\boldsymbol{r}}_\odot = 0 \quad , \quad \ddot{\boldsymbol{r}}_\odot = 0 \quad , \quad \hat{\boldsymbol{r}}_\odot \equiv \hat{\boldsymbol{\imath}} \quad , \quad r_\odot = r_{\odot_e} \tag{11}$$

so that the dimensionless propulsive acceleration vector $\boldsymbol{a}$ is aligned with the Sun-Earth line, that is, $\boldsymbol{a}\times\hat{\boldsymbol{\imath}} = 0$; see Fig. 3. Bearing in mind Eq. (4), the constraint $\boldsymbol{a}\times\hat{\boldsymbol{\imath}} = 0$ amounts to orienting the sail normal along the radial direction or, equivalently, to enforcing the constraints

$$\widetilde{\hat{\boldsymbol{n}}} = \hat{\boldsymbol{r}}_\odot \equiv \hat{\boldsymbol{\imath}} \quad , \quad \widetilde{\theta} = 0 \tag{12}$$

in Eq. (4). The result is

$$\boldsymbol{a} = \boldsymbol{a}_e \triangleq \widetilde{\beta}_e\,\frac{1-\mu}{r_{\odot_e}^2}\,\hat{\boldsymbol{\imath}} \tag{13}$$

where the subscript "e" denotes an equilibrium value. The dimensionless spacecraft position vector $\boldsymbol{r}_e$ at the equilibrium condition is therefore

$$\boldsymbol{r}_e = (r_{\odot_e} - \mu)\,\hat{\boldsymbol{\imath}} \tag{14}$$

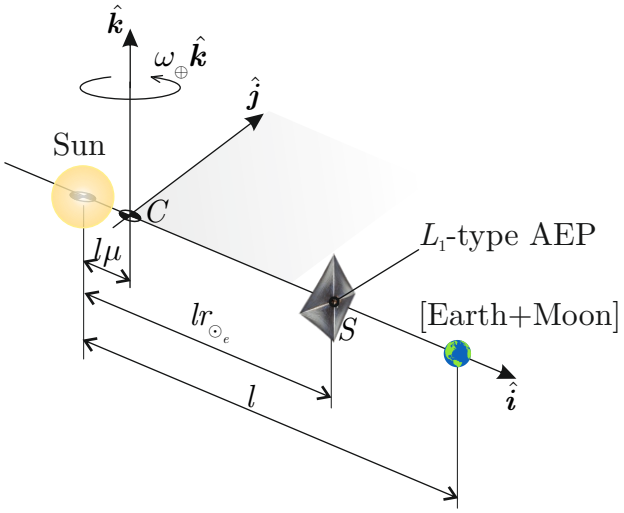

Figure 3: Sketch of an L_1-type AEP in the Sun-[Earth+Moon] CRTBP.

Using Eqs. (11) and (13), Eq. (1) becomes

$$-r_{\odot_e} + \mu + \frac{1-\mu}{r_{\odot_e}^2} - \frac{\mu}{(1-r_{\odot_e})^2} = \widetilde{\beta}_e\,\frac{1-\mu}{r_{\odot_e}^2} \tag{15}$$

so that the required (nominal) wrinkled-sail lightness number $\widetilde{\beta}_e$ necessary to maintain an L_1-type AEP is

$$\widetilde{\beta}_e = 1 - \frac{\mu\, r_{\odot_e}^2}{1-\mu}\left[\frac{r_{\odot_e}}{\mu} + \frac{1}{(1-r_{\odot_e})^2} - 1\right] \tag{16}$$

The variation of the required wrinkled-sail lightness number as a function of the desired Sun-AEP distance $r_{\odot_e}$ is plotted in Fig. 4, while Fig. 5 shows the warning time as a function of $\widetilde{\beta}_e$ and the solar wind speed. Lightness numbers corresponding to the current technology level (on the order of 0.01) may guarantee a warning time of about 70 minutes in case of average solar wind speed ($\simeq 400\,\mathrm{km/s}$), and of about 35 minutes when fast streams (with velocities on the order of $800\,\mathrm{km/s}$) are considered. Assuming a higher-performance sail, with a lightness number of 0.02, (corresponding to the design value of the Solar Orbiter mission with a near-term technology level), the warning time increases to about 80 minutes for an average solar wind speed and about 40 minutes for fast streams.

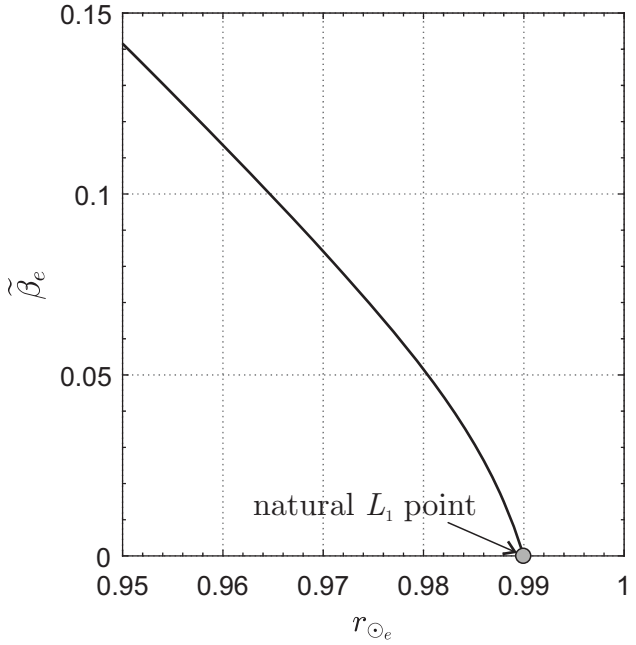

Figure 4: Wrinkled-sail lightness number $\widetilde{\beta}_e$ as a function of dimensionless Sun-AEP distance $r_{\odot_e}$.

Since L_1-type AEPs are known to be intrinsically unstable [33, 42], as is confirmed by the linear stability analysis reported in the remainder of this section, their maintenance requires a suitable control system to be used.

2.1. Linear stability analysis

Consider a perturbed state in which the artificial equilibrium condition is modified as follows

$$\boldsymbol{r} = \boldsymbol{r}_e + \delta\boldsymbol{r} \triangleq (r_{\odot_e} - \mu + x)\,\hat{\boldsymbol{\imath}} + y\,\hat{\boldsymbol{\jmath}} + z\,\hat{\boldsymbol{k}} \tag{17}$$

$$\dot{\boldsymbol{r}} = \delta\dot{\boldsymbol{r}} \triangleq v_x\,\hat{\boldsymbol{\imath}} + v_y\,\hat{\boldsymbol{\jmath}} + v_z\,\hat{\boldsymbol{k}} \tag{18}$$

where $\delta\boldsymbol{r}$ is the dimensionless position vector perturbation (with components $\{x, y, z\}$), and $\delta\dot{\boldsymbol{r}}$ is the dimensionless velocity vector perturbation (with components $\{v_x, v_y, v_z\}$). To analyze the spacecraft perturbed dynamics in the AEP vicinity, introduce the dimensionless state vector $\boldsymbol{x} \in \mathbb{R}^{6\times 1}$ defined as

$$\boldsymbol{x} \triangleq \begin{bmatrix} \delta\boldsymbol{r} \\ \delta\dot{\boldsymbol{r}} \end{bmatrix} \tag{19}$$

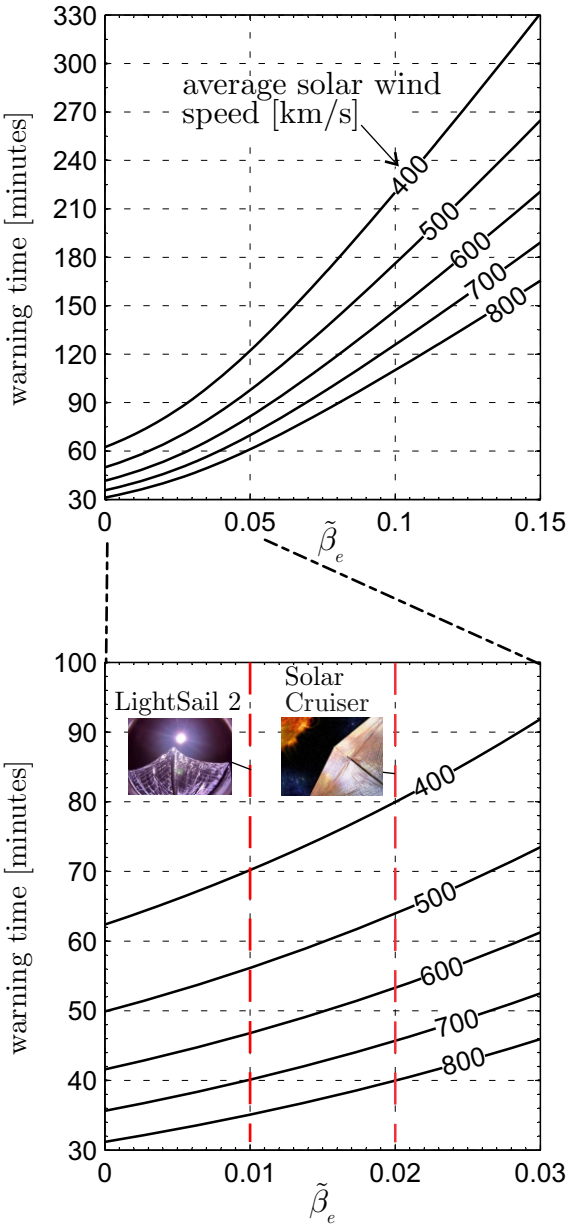

Figure 5: Warning time as a function of the wrinkled-sail lightness number $\widetilde{\beta}_e$ and solar wind (average) speed.

Accordingly, the spacecraft linearized dynamics in the vicinity of an L_1-type AEP can be written as [42]

$$\dot{\boldsymbol{x}} = \mathbb{A}\,\boldsymbol{x} \tag{20}$$

with

$$\mathbb{A} = \begin{bmatrix} \mathbb{O} & \mathbb{I} \\ \mathbb{C} & \mathbb{S} \end{bmatrix} \tag{21}$$

where $\mathbb{O} \in \mathbb{R}^{3\times3}$ is a zero matrix, $\mathbb{I} \in \mathbb{R}^{3\times3}$ is an identity matrix, $\mathbb{S}$ is a skew-symmetric matrix given by

$$\mathbb{S} = \begin{bmatrix} 0 & 2 & 0 \\ -2 & 0 & 0 \\ 0 & 0 & 0 \end{bmatrix} \tag{22}$$

and

$$\mathbb{C} \triangleq \begin{bmatrix} c_1 & 0 & 0 \\ 0 & c_2 & 0 \\ 0 & 0 & c_3 \end{bmatrix} \tag{23}$$

where

$$c_1 \triangleq 1 + \frac{2\,\mu}{(1-r_{\odot_e})^3} + \frac{2\,(1-\mu)}{r_{\odot_e}^3} - 2\,\widetilde{\beta}_e\,\frac{1-\mu}{r_{\odot_e}^3} \tag{24}$$

$$c_2 \triangleq \frac{\mu}{r_{\odot_e}}\left[1 - \frac{1}{(1-r_{\odot_e})^3}\right] \tag{25}$$

$$c_3 \triangleq c_2 - 1 \tag{26}$$

The system described by Eq. (20) is known to be unstable [33, 42], and this is confirmed by Fig. 6, which shows the real parts of the eigenvalues Λ_i (with $i = 1, 2, \ldots, 6$) of matrix $\mathbb{A}$ for $r_{\odot_e} > 0.95$. In particular, matrix $\mathbb{A}$ has four imaginary eigenvalues (Λ_3, Λ_4, Λ_5, Λ_6), one stable eigenvalue (Λ_2) and one unstable eigenvalue (Λ_1). A control system is therefore required for the L_1-type AEP maintenance.

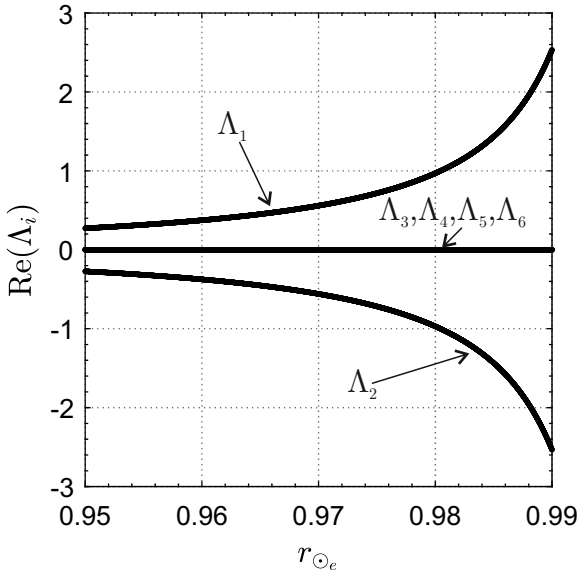

Figure 6: Real part of the eigenvalues Λ_i of matrix $\mathbb{A}$ for different Sun-AEP dimensionless distance $r_{\odot_e}$.

3. Wrinkled-sail controlled dynamics

To analyze the controlled dynamics of a solar sail-based spacecraft placed at an L_1-type AEP, introduce a right-handed body-fixed reference frame $\mathcal{T}_B(S; \hat{\boldsymbol{n}}, \hat{\boldsymbol{p}}, \hat{\boldsymbol{q}})$, with origin at the spacecraft center of mass S, which also coincides with the solar sail center of mass. The unit vectors $\hat{\boldsymbol{p}}$ and $\hat{\boldsymbol{q}}$ are assumed to lie along the principal axes of inertia of the (ideal) unwrinkled-sail.

In the nominal (unperturbed) equilibrium condition, the unwrinkled-sail is placed at the L_1-type AEP with a Sun-facing attitude, so that the normal unit vector $\hat{\boldsymbol{n}}$ is along the radial direction, and $\hat{\boldsymbol{p}}$ lies on the Ecliptic. Consider now a second right-handed body-fixed reference frame $\widetilde{\mathcal{T}}_B(S; \widetilde{\hat{\boldsymbol{n}}}, \widetilde{\hat{\boldsymbol{p}}}, \widetilde{\hat{\boldsymbol{q}}})$, in which $\widetilde{\hat{\boldsymbol{p}}}$, in its turn, is on the Ecliptic. The reference frame $\mathcal{T}_B$ can be overlapped to $\widetilde{\mathcal{T}}_B$ by means of two rotations, that is, i) a clockwise rotation of an angle ψ_0 around the unit the vector $\hat{\boldsymbol{n}}$ so that $\hat{\boldsymbol{p}}$ coincides with $\widetilde{\hat{\boldsymbol{p}}}$, and ii) a counterclockwise rotation of an angle α_0 around the unit vector $\widetilde{\hat{\boldsymbol{p}}}$; see Fig. 7.

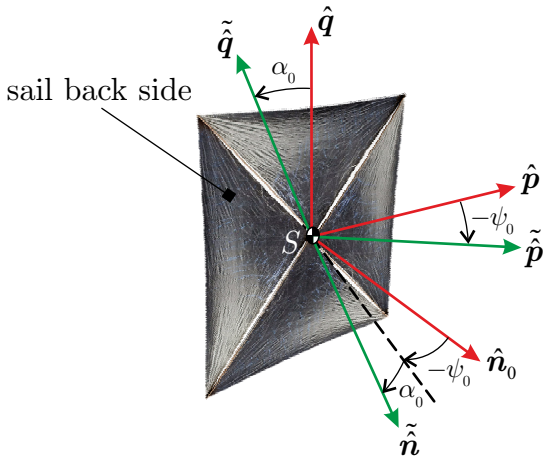

Figure 7: Sketch of the two body reference frames $\mathcal{T}_B$ (red) and $\widetilde{\mathcal{T}_B}$ (green), and of the Euler angles $\{\psi_0, \alpha_0\}$.

The rotation matrix $\mathbb{R}_{\mathcal{T}_B}^{\widetilde{\mathcal{T}_B}}$ between the reference frames $\mathcal{T}_B$ and $\widetilde{\mathcal{T}}_B$ is therefore

$$\mathbb{R}_{\mathcal{T}_B}^{\widetilde{\mathcal{T}_B}} = \mathbb{R}_2(\alpha_0)\,\mathbb{R}_3(-\psi_0) = \begin{bmatrix} \cos\psi_0\cos\alpha_0 & -\sin\psi_0\cos\alpha_0 & -\sin\alpha_0 \\ \sin\psi_0 & \cos\psi_0 & 0 \\ \cos\psi_0\sin\alpha_0 & -\sin\psi_0\sin\alpha_0 & \cos\alpha_0 \end{bmatrix} \tag{27}$$

To estimate the Euler's angles α_0 and ψ_0, first note that $[\widetilde{\hat{\boldsymbol{n}}}]_{\widetilde{\mathcal{T}}_B} = [1 \quad 0 \quad 0]^{\mathrm{T}}$. From Eq. (27), we get

$$[\widetilde{\hat{\boldsymbol{n}}}]_{\mathcal{T}_B} = \left(\mathbb{R}_{\mathcal{T}_B}^{\widetilde{\mathcal{T}_B}}\right)^{\mathrm{T}} \begin{bmatrix} 1 \\ 0 \\ 0 \end{bmatrix} = \begin{bmatrix} \cos\psi_0\cos\alpha_0 \\ -\sin\psi_0\cos\alpha_0 \\ -\sin\alpha_0 \end{bmatrix} \tag{28}$$

Based on the experimental measurements described in Ref. [44], the components of $\widetilde{\hat{\boldsymbol{n}}}$ in $\mathcal{T}_B$ may be estimated (more details are given in the Appendix) as follows

$$[\widetilde{\hat{\boldsymbol{n}}}]_{\mathcal{T}_B} = [0.991 \quad -0.123 \quad -0.055]^{\mathrm{T}} \tag{29}$$

so that, combining Eqs. (28) and (29), the values of angles α_0 and ψ_0 are

$$\alpha_0 = 3.153\,\mathrm{deg} \tag{30}$$

$$\psi_0 = 7.021\,\mathrm{deg} \tag{31}$$

Note that the pair $\{\alpha_0, \psi_0\}$ fully defines the orientation of $\widetilde{\mathcal{T}}_B$ with respect to $\mathcal{T}_B$, thus allowing the dynamics of a wrinkled-sail to be written in a similar way as that of an unwrinkled-sail.

The orientation of $\widetilde{\mathcal{T}}_B$ with respect to the synodic reference frame $\mathcal{T}_S$ is defined through the azimuth ψ and elevation α angles; see Fig. 8. More precisely, α is the angle between the direction of $\widetilde{\hat{\boldsymbol{n}}}$ and the Ecliptic, while ψ is the angle between the direction of $\hat{\boldsymbol{i}}$ and the projection of $\widetilde{\hat{\boldsymbol{n}}}$ on the Ecliptic. In this case, the rotation matrix $\mathbb{R}_{\mathcal{T}_S}^{\widetilde{\mathcal{T}}_B}$ from the synodic reference frame $\mathcal{T}_S$ to the body reference frame $\widetilde{\mathcal{T}}_B$ may be decomposed in two elementary rotations, that is, i) a counterclockwise rotation of an angle ψ around the unit vector $\hat{\boldsymbol{k}}$ to overlap $\hat{\boldsymbol{i}}$ with the projection of $\widetilde{\hat{\boldsymbol{n}}}$ on the Ecliptic, and ii) a counterclockwise rotation of an angle α around the rotated $\hat{\boldsymbol{p}}$ unit vector, viz.

$$\mathbb{R}_{\mathcal{T}_S}^{\widetilde{\mathcal{T}}_B} = \mathbb{R}_2(\alpha)\,\mathbb{R}_3(\psi) = \begin{bmatrix} \cos\psi\cos\alpha & \sin\psi\cos\alpha & -\sin\alpha \\ -\sin\psi & \cos\psi & 0 \\ \cos\psi\sin\alpha & \sin\psi\sin\alpha & \cos\alpha \end{bmatrix} \tag{32}$$

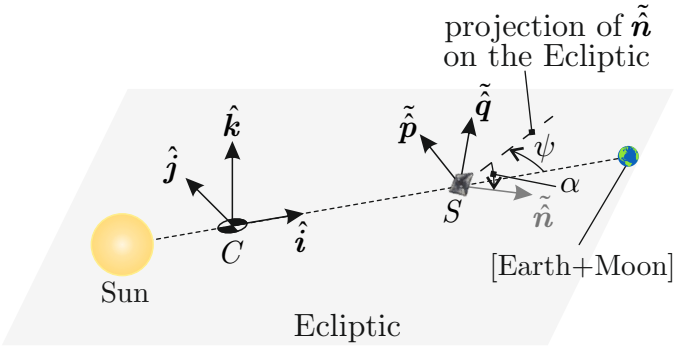

Figure 8: Orientation of the body reference frame $\widetilde{\mathcal{T}}_B$ with respect to the synodic reference frame $\mathcal{T}_S$.

The components of $\widetilde{\hat{\boldsymbol{n}}}$ in the synodic reference frame are therefore

$$[\widetilde{\hat{\boldsymbol{n}}}]_{\mathcal{T}_S} = \left(\mathbb{R}_{\mathcal{T}_S}^{\widetilde{\mathcal{T}}_B}\right)^{\mathrm{T}} \begin{bmatrix} 1 \\ 0 \\ 0 \end{bmatrix} = \begin{bmatrix} \cos\psi\cos\alpha \\ \sin\psi\cos\alpha \\ -\sin\alpha \end{bmatrix} \tag{33}$$

so that, bearing in mind Eq. (4), the components of the propulsive acceleration vector $\boldsymbol{a}$ in $\mathcal{T}_S$ are given by

$$[\boldsymbol{a}]_{\mathcal{T}_S} = \widetilde{\beta}\,\frac{1-\mu}{r_{\odot}^2}\,\frac{\cos\alpha\cos\psi}{b_1+b_2+b_3} \begin{bmatrix} b_1 + b_2\cos^2\alpha\cos^2\psi + b_3\cos\alpha\cos\psi \\ \sin\psi\cos\alpha\,(b_2\cos\alpha\cos\psi + b_3) \\ -\sin\alpha\,(b_2\cos\alpha\cos\psi + b_3) \end{bmatrix} \tag{34}$$

Note that the expression of the propulsive acceleration vector along the (nominal) equilibrium point $\boldsymbol{a}_e$, given by Eq. (13), can be recovered from Eq. (34) by enforcing the conditions

$$r_{\odot} = r_{\odot_e} \quad , \quad \widetilde{\beta} = \widetilde{\beta}_e \quad , \quad \psi = \psi_e \triangleq 0 \quad , \quad \alpha = \alpha_e \triangleq 0 \tag{35}$$

where $\widetilde{\beta}_e$ is given by Eq. (16) as a function of the L_1-type AEP position.

Consider now a perturbed state around the equilibrium condition, in which

$$r_{\odot} = \sqrt{(r_{\odot_e}+x)^2 + y^2 + z^2} \quad , \quad \psi = \psi_e + \widetilde{\psi} \equiv \widetilde{\psi} \quad , \quad \alpha = \alpha_e + \widetilde{\alpha} \equiv \widetilde{\alpha} \tag{36}$$

with $\widetilde{\psi} \ll 1$ and $\widetilde{\alpha} \ll 1$. The components of $\boldsymbol{a}$ in Eq. (34) can be linearized under the assumption that the spacecraft remains in the vicinity of the L_1-type AEP, that is, by enforcing the conditions

$$r_{\odot}^2 \simeq \frac{r_{\odot_e}^2}{(1-2x/r_{\odot_e})} \quad , \quad \cos\alpha \equiv \cos\psi \simeq 1 \quad , \quad \sin\psi \simeq \widetilde{\psi} \quad , \quad \sin\alpha \simeq \widetilde{\alpha} \tag{37}$$

The result is

$$[\boldsymbol{a}]_{\mathcal{T}_S} \simeq \widetilde{\beta}\,\frac{1-\mu}{r_{\odot_e}^2}\left(1-\frac{2x}{r_{\odot_e}}\right) \begin{bmatrix} 1 \\ \widetilde{\psi}\,\dfrac{b_2+b_3}{b_1+b_2+b_3} \\ -\widetilde{\alpha}\,\dfrac{b_2+b_3}{b_1+b_2+b_3} \end{bmatrix} \tag{38}$$

Assume now that the solar sail is equipped with RCDs, that is, a part of the sail area is covered by panels whose optical properties can be varied within a prescribed range [42]. In that case, both the direction and the magnitude of $\boldsymbol{a}$ can be controlled. This corresponds to assuming, in Eq. (38), that the angles $\{\widetilde{\alpha}, \widetilde{\psi}\}$ and the sail lightness number play the role of control variables. In particular, $\widetilde{\beta}$ can be written as

$$\widetilde{\beta} = \widetilde{\beta}_e + \delta\widetilde{\beta} \tag{39}$$

where $\delta\widetilde{\beta}$ is the sail lightness number variation due to the RCD-based control system.

Substituting Eqs. (38)-(39) into Eq. (1), subtracting the equilibrium solution given by Eq. (15) and neglecting the second order terms, the linearized equation of motion (neglecting any disturbance source) is

$$\dot{\boldsymbol{x}} = \mathbb{A}\,\boldsymbol{x} + \mathbb{B}\,\boldsymbol{u} \tag{40}$$

where $\mathbb{A}$ is given by Eq. (21), matrix $\mathbb{B}$ is defined as

$$\mathbb{B} \triangleq \begin{bmatrix} \mathbb{O} \\ \mathbb{B}_v \end{bmatrix} \tag{41}$$

in which

$$\mathbb{B}_v = \begin{bmatrix} 1 & 0 & 0 \\ 0 & \widetilde{\beta}_e \dfrac{b_2+b_3}{b_1+b_2+b_3} & 0 \\ 0 & 0 & -\widetilde{\beta}_e \dfrac{b_2+b_3}{b_1+b_2+b_3} \end{bmatrix} \tag{42}$$

and $\boldsymbol{u}$ is the control vector defined as

$$\boldsymbol{u} = [\delta\widetilde{\beta}, \quad \widetilde{\psi}, \quad \widetilde{\alpha}]^{\mathrm{T}} \tag{43}$$

In particular, $\widetilde{\psi}$ and $\widetilde{\alpha}$ are actually virtual inputs since they can be generated by means of suitable torques, as will be discussed later.

3.1. Control law design

Since L_1-type AEPs are unstable, a suitable feedback control law is necessary to maintain the spacecraft at the desired position. A possible and effective choice is offered by a full-state feedback control law, in the form

$$\boldsymbol{u} = -\mathbb{K}\,\boldsymbol{x} \tag{44}$$

In that case, the 3×6 matrix $\mathbb{K}$ may be obtained by solving the associated linear quadratic problem, as suggested in Ref. [42]. To simplify the control system structure, in this paper we face the problem by avoiding the need of measuring the full system state, as required by Eq. (44). More precisely, the measured variables are written as

$$\boldsymbol{y} = \mathbb{C}\,\boldsymbol{x} \tag{45}$$

where $\boldsymbol{y} \in \mathbb{R}^p$, with $p < 6$, that is, the number of outputs is less than the number of states, and, accordingly, $\mathbb{C}$ is a $p \times 6$ matrix. Assume also that the linearized (vectorial) equation of motion (40) is modified as

$$\dot{\boldsymbol{x}} = \mathbb{A}\,\boldsymbol{x} + \mathbb{B}\,\boldsymbol{u} + \mathbb{D}\,\boldsymbol{d} \tag{46}$$

where $\boldsymbol{d}$ is a vector, function of the time, which models the presence of disturbances, while $\mathbb{D}$ defines which state is actually affected by some disturbance. A simple control law is sought in the form

$$\boldsymbol{u} = -\mathbb{K}\,\boldsymbol{y} \tag{47}$$

where $\mathbb{K}$ is a $3 \times p$ constant gain matrix. Substituting Eqs. (47) and (45) into Eq. (46) yields

$$\dot{\boldsymbol{x}} = (\mathbb{A} - \mathbb{B}\mathbb{K}\mathbb{C})\boldsymbol{x} + \mathbb{D}\,\boldsymbol{d} \tag{48}$$

whose dynamics clearly depends on the eigenvalues of $(\mathbb{A} - \mathbb{B}\mathbb{K}\mathbb{C})$. It is well known that the solution to the static output feedback problem of Eq. (47) is a rather complex task to solve, although it is very attractive in practical applications as it allows controllers with a prescribed structure to be obtained. An effective algorithm [45] exists for calculating an H_∞ static output-feedback control that solves the so called bounded L_2 gain design problem in the form of Eq. (47), that is, which defines a stable closed-loop system whose L_2 gain is attenuated by a factor $\gamma > 0$, such that

$$\frac{\int_0^{+\infty} (\boldsymbol{x}^{\mathrm{T}}\mathbb{Q}\,\boldsymbol{x} + \boldsymbol{u}^{\mathrm{T}}\mathbb{R}\,\boldsymbol{u})\,\mathrm{d}t}{\int_0^{+\infty} (\boldsymbol{d}^{\mathrm{T}}\,\boldsymbol{d})\,\mathrm{d}t} \leq \gamma^2 \tag{49}$$

where $\mathbb{Q} \geq 0$ and $\mathbb{R} > 0$ are suitable symmetric matrices. Necessary and sufficient conditions for the existence of a solution to the previous problem are as follows [45]: 1) the pair $(\mathbb{A}, \mathbb{B})$ is stabilizable, 2) the pair $(\mathbb{A}, \mathbb{C})$ is detectable, and 3) there exist matrices $\mathbb{K}$ and $\mathbb{L}$ such that

$$\mathbb{K}\mathbb{C} = \mathbb{R}^{-1}(\mathbb{B}^{\mathrm{T}}\mathbb{P} + \mathbb{L}) \tag{50}$$

where $\mathbb{P} = \mathbb{P}^{\mathrm{T}}$ is a solution of the algebraic Riccati equation

$$\mathbb{P}\mathbb{A} + \mathbb{A}^{\mathrm{T}}\mathbb{P} + \mathbb{Q} + \mathbb{P}\mathbb{D}\mathbb{D}^{\mathrm{T}}\mathbb{P}/\gamma^2 - \mathbb{P}\mathbb{B}\mathbb{R}^{-1}\mathbb{B}^{\mathrm{T}}\mathbb{P} + \mathbb{L}^{\mathrm{T}}\mathbb{R}^{-1}\mathbb{L} = 0 \tag{51}$$

An algorithm for finding a solution to the bounded L_2 gain problem is reported in Ref. [45], to which the reader is referred for further details. To simplify the problem, it is assumed that $\mathbb{Q} = \mathbb{C}^{\mathrm{T}}\mathbb{C}$, so that the designer is only faced with a suitable choice of the weighting matrix $\mathbb{R}$.

3.2. Control torque estimation

The control torques required by the control system may be estimated from the Euler's equations, observing that the angular velocity $\boldsymbol{\omega}$ of the body reference frame $\mathcal{T}_B$ with respect to a generic inertial frame is

$$\boldsymbol{\omega} = \boldsymbol{\omega}_{BS} + \boldsymbol{\omega}_{\oplus} \tag{52}$$

where $\boldsymbol{\omega}_{BS}$ is the angular velocity of $\mathcal{T}_B$ relative to the synodic reference frame $\mathcal{T}_S$ and $\boldsymbol{\omega}_{\oplus}$ is the angular velocity of the synodic frame $\mathcal{T}_S$ with respect to an inertial reference frame. The components of $\boldsymbol{\omega}_{\oplus}$ in $\mathcal{T}_B$ are obtained from the rotation matrices (27) and (32) as

$$[\boldsymbol{\omega}_{\oplus}]_{\mathcal{T}_B} = \mathbb{R}_{\widetilde{\mathcal{T}}_B}^{\mathcal{T}_B}\,\mathbb{R}_{\mathcal{T}_S}^{\widetilde{\mathcal{T}}_B} \begin{bmatrix} 0 \\ 0 \\ \omega_{\oplus} \end{bmatrix} = \begin{bmatrix} -\omega_{\oplus}\sin\widetilde{\alpha}\cos\psi_0\cos\alpha_0 + \omega_{\oplus}\cos\widetilde{\alpha}\cos\psi_0\sin\alpha_0 \\ \omega_{\oplus}\sin\widetilde{\alpha}\sin\psi_0\cos\alpha_0 - \omega_{\oplus}\cos\widetilde{\alpha}\sin\psi_0\sin\alpha_0 \\ \omega_{\oplus}\sin\widetilde{\alpha}\sin\alpha_0 + \omega_{\oplus}\cos\widetilde{\alpha}\cos\alpha_0 \end{bmatrix} \tag{53}$$

while, with the aid of Fig. 8, the angular velocity $\boldsymbol{\omega}_{BS}$ can be written as

$$\boldsymbol{\omega}_{BS} = \dot{\widetilde{\psi}}\,\hat{\boldsymbol{k}} + \dot{\widetilde{\alpha}}\,\widetilde{\boldsymbol{p}} \tag{54}$$

from which

$$[\boldsymbol{\omega}_{BS}]_{\mathcal{T}_B} = \dot{\widetilde{\psi}}\,\mathbb{R}_{\widetilde{\mathcal{T}}_B}^{\mathcal{T}_B}\,\mathbb{R}_{\mathcal{T}_S}^{\widetilde{\mathcal{T}}_B} \begin{bmatrix} 0 \\ 0 \\ 1 \end{bmatrix} + \dot{\widetilde{\alpha}}\,\mathbb{R}_{\widetilde{\mathcal{T}}_B}^{\mathcal{T}_B} \begin{bmatrix} 0 \\ 1 \\ 0 \end{bmatrix} = \begin{bmatrix} -\dot{\widetilde{\psi}}\sin\widetilde{\alpha}\cos\psi_0\cos\alpha_0 + \dot{\widetilde{\psi}}\cos\widetilde{\alpha}\cos\psi_0\sin\alpha_0 + \dot{\widetilde{\alpha}}\sin\psi_0 \\ \dot{\widetilde{\psi}}\sin\widetilde{\alpha}\sin\psi_0\cos\alpha_0 - \dot{\widetilde{\psi}}\cos\widetilde{\alpha}\sin\psi_0\sin\alpha_0 + \dot{\widetilde{\alpha}}\cos\psi_0 \\ \dot{\widetilde{\psi}}\sin\widetilde{\alpha}\sin\alpha_0 + \dot{\widetilde{\psi}}\cos\widetilde{\alpha}\cos\alpha_0 \end{bmatrix} \tag{55}$$

Finally, the (linearized) components of $\boldsymbol{\omega}$ in $\mathcal{T}_B$ are

$$[\boldsymbol{\omega}]_{\mathcal{T}_B} \triangleq \begin{bmatrix} \omega_1 \\ \omega_2 \\ \omega_3 \end{bmatrix} \simeq \begin{bmatrix} -\widetilde{\alpha}\,(\omega_{\oplus} + \dot{\widetilde{\psi}})\cos\psi_0\cos\alpha_0 + (\omega_{\oplus} + \dot{\widetilde{\psi}})\cos\psi_0\sin\alpha_0 + \dot{\widetilde{\alpha}}\sin\psi_0 \\ \widetilde{\alpha}\,(\omega_{\oplus} + \dot{\widetilde{\psi}})\sin\psi_0\cos\alpha_0 - (\omega_{\oplus} + \dot{\widetilde{\psi}})\sin\psi_0\sin\alpha_0 + \dot{\widetilde{\alpha}}\cos\psi_0 \\ \widetilde{\alpha}\,(\omega_{\oplus} + \dot{\widetilde{\psi}})\sin\alpha_0 + (\omega_{\oplus} + \dot{\widetilde{\psi}})\cos\alpha_0 \end{bmatrix} \tag{56}$$

where α_0 and ψ_0 are given by Eqs. (30)-(31), while the time variations of the Euler angles are obtained from the controlled outputs, once the non-linear equation of motion (1) has been numerically solved. From Euler's equations, the required control torque vector $[\boldsymbol{M}]_{\mathcal{T}_B} = [M_1,\, M_2,\, M_3]^{\mathrm{T}}$ is

$$I_1\,\dot{\omega}_1 + (I_3 - I_2)\,\omega_2\,\omega_3 = M_1 \tag{57}$$

$$I_2\,\dot{\omega}_2 + (I_1 - I_3)\,\omega_1\,\omega_3 = M_2 \tag{58}$$

$$I_3\,\dot{\omega}_3 + (I_2 - I_1)\,\omega_1\,\omega_2 = M_3 \tag{59}$$

where $\{I_1, I_2, I_3\}$ are the spacecraft principal moments of inertia in $\mathcal{T}_B$.

3.3. Solar radiation-induced force given by RCDs

To fully define the controlled dynamics of the spacecraft, the force produced by a set of RCDs in their on- or off-state must be modelled. To that end, the optical properties in the on-state are often assumed to be equal to those of the sail membrane [40], that is

$$\rho_{s,\mathrm{on}} = \rho_s \tag{60}$$

$$\rho_{d,\mathrm{on}} = \rho_d \tag{61}$$

$$\kappa_{\mathrm{on}} = \kappa \tag{62}$$

The optical properties of the RCDs in the off-state must be determined experimentally, but the fraction of light that is not absorbed is, to a first order, assumed to be all diffusely reflected, that is

$$\rho_{s,\mathrm{off}} = 0 \tag{63}$$

$$\rho_{d,\mathrm{off}} = 1 - \kappa \tag{64}$$

where, according to Ref. [38], the absorption coefficients in the on- and off-states are considered to be equal. The force coefficients b_i, defined in Eqs. (6), can be therefore specialized to the RCDs in their on- and off-states. The results are summarized in Table 1.

Table 1: Force coefficients of sail and RCDs in their two possible states.

	b_1	b_2	b_3
Sail	$\kappa + \rho_d$	$2\,\rho_s$	$B_f\,\rho_d$
RCD on	$\kappa + \rho_d$	$2\,\rho_s$	$B_f\,\rho_d$
RCD off	1	0	$B_f\,(1-\kappa)$

Using the optical properties of Eq. (9), the numerical values of $\{b_1, b_2, b_3\}$ are reported in Tab. 2.

Table 2: Numerical values of the force coefficients of the sail and the RCDs in their two possible states.

	b_1	b_2	b_3
Sail	0.1901	1.6198	0.0791
RCD on	0.1901	1.6198	0.0791
RCD off	1	0	0.7189

With the aid of the model discussed in the Appendix, the expression of the solar radiation-induced force $\boldsymbol{T}_{\mathrm{on}}$ given by a set of RCDs in their on- or off- state is

$$\boldsymbol{T}_{\mathrm{on}} = P_{\oplus}\,A_{\mathrm{on}}\cos\widetilde{\theta}\left[b_{1_{\mathrm{on}}}\,\hat{\boldsymbol{r}}_{\odot} + \left(b_{2_{\mathrm{on}}}\cos\widetilde{\theta} + b_{3_{\mathrm{on}}}\right)\widetilde{\hat{\boldsymbol{n}}}\right] \tag{65}$$

$$\boldsymbol{T}_{\mathrm{off}} = P_{\oplus}\,A_{\mathrm{off}}\cos\widetilde{\theta}\left(\hat{\boldsymbol{r}}_{\odot} + b_{3_{\mathrm{off}}}\,\widetilde{\hat{\boldsymbol{n}}}\right) \tag{66}$$

3.4. Preliminary solar sail sizing

When the time history of the control inputs is known from the numerical simulations, it is possible to carry out a preliminary sizing of the solar sail by evaluating the total sail area and the fraction of surface that must be covered with RCDs. To that end, consider a square sail with side length $2\,L$. Paralleling the procedure described in Ref. [40], a set of RCDs (of area $2\,A_1$) must be mounted on the central part of the sail to control the value of the lightness number; see Fig. 9.

In the nominal (equilibrium) configuration, half of these RCDs should be switched on, so that $\widetilde{\beta}$ can be either increased or decreased according to the position and velocity errors along the $\hat{\boldsymbol{i}}$-axis. When some of these devices are switched either on or off, a symmetric configuration must always be guaranteed, so that the sail is in a torque-free condition. The angles $\{\widetilde{\psi}, \widetilde{\alpha}\}$, which define the orientation of the unit vector $\widetilde{\hat{\boldsymbol{n}}}$, are controlled by means of four sets of RCDs (each one of area A_2) mounted along the four sides of the sail. If the sail is in its nominal (equilibrium) configuration, the RCDs are in an off-state to avoid any power

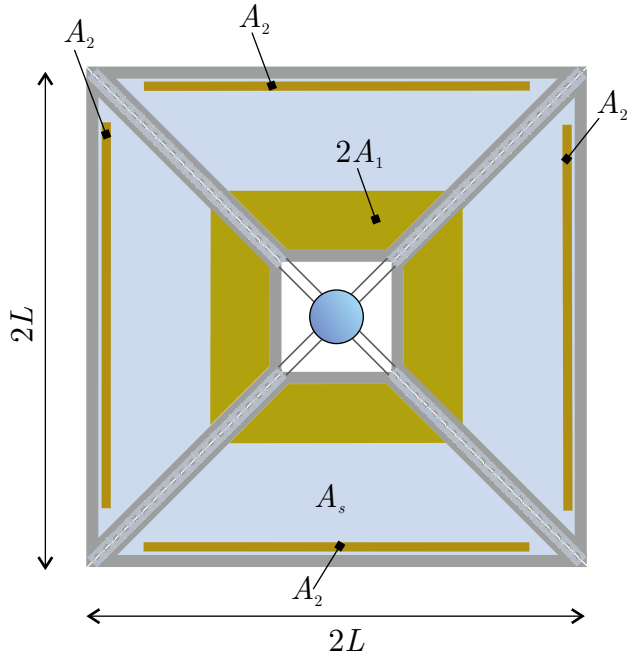

Figure 9: Sketch of the solar sail design with RCDs.

consumption. When a torque must be applied to the spacecraft, a set of RCDs is switched on, so that the solar radiation pressure acting on them increases, while those on the opposite side of the sail remain in their off-state. This causes the generation of a control torque with respect to the spacecraft center of mass S.

Let A_s be the area of the sail film not covered by any RCD. With the aid of Fig. 9, the (nominal) unwrinkled-sail area is

$$A = A_s + 2A_1 + 4A_2 \tag{67}$$

while the effective area that contributes to thrust is

$$\widetilde{A} = \widetilde{A}_s + 2\,\widetilde{A}_1 + 4\,\widetilde{A}_2 = (A_s + \delta A_s) + 2(A_1 + \delta A_1) + 4(A_2 + \delta A_2) \tag{68}$$

Each area fraction is assumed to be subjected to the same relative variation that the whole sail undergoes due to loading and wrinkles, that is

$$\frac{\delta A_s}{A_s} = \frac{\delta A_1}{A_1} = \frac{\delta A_2}{A_2} = k < 0 \tag{69}$$

where $k \simeq -0.126$ is the output of the experiment described in Ref. [44].

To estimate A_s, A_1 and A_2, recall that the sail lightness number $\widetilde{\beta}$ can be expressed as [40]

$$\widetilde{\beta} = \frac{\sigma_{\rm cr}\,(\eta_s\,\widetilde{A}_s + \eta_{\rm off}\,\widetilde{A}_{\rm off} + \eta_{\rm on}\,\widetilde{A}_{\rm on})}{m} \tag{70}$$

where $\sigma_{\rm cr} = 1.56\,{\rm g/m^2}$ is a reference parameter, $\widetilde{A}_{\rm on}$ is the (wrinkled) area of RCDs in the on-state, $\widetilde{A}_{\rm off}$ is the (wrinkled) area of RCDs in the off-state, while $\eta_{\rm on}$, $\eta_{\rm off}$ and η_s measure the efficiency of RCDs and sail. The latter values may be calculated from $\eta = (b_1 + b_2 + b_3)/2$ with the aid of Tables 1 and 2, and the result is $\eta_s = \eta_{\rm on} = 0.9445$ and $\eta_{\rm off} = 0.8595$. The total mass of the spacecraft is a function of the sail loading σ, defined as the ratio of the mass to the reflective area of the membrane. According to Ref. [59], $\sigma_s = 5.68\,{\rm g/m^2}$ is assumed for the sail membrane, while $\sigma_{\rm RCD} = 80\,{\rm g/m^2}$ is used for RCD panels [60]. The spacecraft mass is therefore

$$m = \sigma_s A_s + \sigma_{\rm RCD}\,(2A_1 + 4A_2) + m_{\rm PL} \tag{71}$$

where $m_{\rm PL}$ is the mass of the rest of the spacecraft, that is, the payload mass.

Consider now the nominal (equilibrium) configuration, with the spacecraft placed at the L_1-type AEP. In this case, the RCDs covering one half of the total area $2\widetilde{A}_1$ and devoted to the $\widetilde{\beta}$-control are in the on-state, while the others are switched off. Moreover, the RCDs devoted to the attitude control are all in the off-state, since no torques is required for orbital maintenance. The overall lightness number in the equilibrium configuration is therefore obtained by substituting

$$\widetilde{A}_{\mathrm{on}_e} = \widetilde{A}_{\mathrm{on}_e} \triangleq \widetilde{A}_1 \quad , \quad \widetilde{A}_{\mathrm{off}} = \widetilde{A}_{\mathrm{off}_e} \triangleq \widetilde{A}_1 + 4\,\widetilde{A}_2 \tag{72}$$

into Eq. (70). With the aid of Eq. (71), we obtain

$$\widetilde{\beta}_e = \frac{\sigma_{\rm cr}\left[\eta_s\, A_s(1+k) + \eta_{\rm on}\, A_1(1+k) + \eta_{\rm off}\, A_1(1+k) + \eta_{\rm off}\, 4A_2(1+k)\right]}{\sigma_s A_s + \sigma_{\rm RCD}\,(2A_1 + 4A_2) + m_{\rm PL}} \tag{73}$$

The sail, in its nominal configuration, may vary its lightness number using the RCDs. The condition $\widetilde{\beta} = \widetilde{\beta}_{\max}$ corresponds to when the RCDs covering the central zone of the sail, with area $2A_1$, are in their on-state. Although the lightness number is also affected by the RCDs devoted to attitude control, their total area is small, so that this contribution is neglected. Therefore, the maximum value of the lightness number comes from Eq. (70) when $\widetilde{A}_{\rm on} = 2\,\widetilde{A}_1$ and $\widetilde{A}_{\rm off} = 4\,\widetilde{A}_2$. The result is

$$\widetilde{\beta}_{\max} = \frac{\sigma_{\rm cr}\left[\eta_s\, A_s(1+k) + 2\,\eta_{\rm on}\, A_1(1+k)\right]}{\sigma_s A_s + \sigma_{\rm RCD}\,(2A_1 + 4A_2) + m_{\rm PL}} \tag{74}$$

Note that Eqs. (73) and (74) provide two equations in the three unknowns A_s, A_1 and A_2. A third independent equation is therefore necessary to solve the problem. This additional equation may be obtained observing that the required control torque is a function of the RCD area and of the lever arm, which depends on the sail geometry. An iterative process is therefore necessary to complete the preliminary solar sail sizing. Since the RCDs devoted to attitude control are mounted at the sail edges, the lever arm for each set of RCDs is about equal to L (one half the sail side length), see Fig. 9. When a control torque has to be generated, one set of these RCDs is switched on, while the symmetric set is kept off, and the resultant control torque $\boldsymbol{M}$ on the sail is

$$\boldsymbol{M} = \boldsymbol{L} \times \boldsymbol{T}_{\rm on} - \boldsymbol{L} \times \boldsymbol{T}_{\rm off} \tag{75}$$

where $\boldsymbol{L}$ is the center of mass-RCD vector (of magnitude L), and $\boldsymbol{T}_{\rm on}$ (or $\boldsymbol{T}_{\rm off}$) is the solar radiation-induced force due to the switched-on (or switched-off) RCDs. Recall that $\boldsymbol{T}_{\rm on}$ and $\boldsymbol{T}_{\rm off}$ are given by Eqs. (65) and (66) where $\widetilde{A}_{\rm on} = \widetilde{A}_{\rm off} = A_2$.

4. Case study

The previous static output feedback solution to the bounded L_2 gain problem is now simulated in a potential mission scenario. The Sun-AEP distance is set equal to $l\,r_{\odot_e} = 0.98872\,\mathrm{au}$, that is, the AEP is shifted towards the Sun of about 189 840 km with respect to the natural Lagrangian point L_1 [42]. Assuming an average solar wind speed of 400 km/s, such an AEP guarantees an early warning time of about 1 hour and 10 minutes, while a very fast stream travelling at 800 km/s would be detected about 35 minutes before it reaches the Earth; see Fig. 5. Bearing in mind Eq. (16), the lightness number required to keep the spacecraft in equilibrium at the desired distance is about $\widetilde{\beta}_e = 0.0101$. Recall that the reference dynamics is described by Eq. (46), where we assume unitary disturbances acting along the three directions $\{x, y, z\}$, that is

$$\mathbb{D} = \begin{bmatrix} \mathbb{I} \\ \mathbb{O} \end{bmatrix} \tag{76}$$

where $\mathbb{I} \in \mathbb{R}^{3\times 3}$ is an identity matrix and $\mathbb{O} \in \mathbb{R}^{3\times 3}$ is a zero matrix. In addition, from Eq. (21), the state matrix is

$$\mathbb{A} = \begin{bmatrix} 0 & 0 & 0 & 1.0000 & 0 & 0 \\ 0 & 0 & 0 & 0 & 1.0000 & 0 \\ 0 & 0 & 0 & 0 & 0 & 1.0000 \\ 7.2851 & 0 & 0 & 0 & 2.0000 & 0 \\ 0 & -2.1425 & 0 & -2.0000 & 0 & 0 \\ 0 & 0 & -3.1425 & 0 & 0 & 0 \end{bmatrix} \tag{77}$$

from which it is clear that the sail dynamics along z in uncoupled from that along x and y. The controlled output vector is chosen as $\boldsymbol{y} = [x,\, v_x,\, v_z]^{\mathrm{T}}$, that is

$$\mathbb{C} = \begin{bmatrix} 1 & 0 & 0 & 0 & 0 & 0 \\ 0 & 0 & 0 & 1 & 0 & 0 \\ 0 & 0 & 0 & 0 & 0 & 1 \end{bmatrix} \tag{78}$$

Bearing in mind that $\mathbb{Q} = \mathbb{C}^{\mathrm{T}}\mathbb{C}$, with a trial-and-error procedure the weighting matrix of Eq. (49) is chosen as $\mathbb{R} = \mathrm{diag}\,(0.3, 10^{-4}, 10^{-5})$, where $\mathrm{diag}(\cdot)$ is a diagonal matrix. The output-feedback algorithm provides

$$\mathbb{K} = \begin{bmatrix} 10.2211 & 4.2247 & 0 \\ 157.2892 & 17.7268 & 0 \\ 0 & 0 & -311.4142 \end{bmatrix} \tag{79}$$

and the closed-loop poles are

$$\lambda_{1,2} = -0.7817 \pm 1.6157\, j\,, \quad \lambda_{3,4} = -1.3791 \pm 0.4544\, j\,, \quad \lambda_{5,6} = -1.4470 \pm 1.0241\, j \tag{80}$$

The static output feedback controller provides a well-damped dynamics and is able to move the solar sail toward the desired AEP. However, in an attempt of further simplifying the control law, assume now that $\boldsymbol{u} = [\delta\widetilde{\beta},\ \widetilde{\alpha}]^{\mathrm{T}}$, thus neglecting the virtual input $\widetilde{\psi}$. As a result, the control system reduces to a 3×2 gain matrix. Using again a trial-and-error procedure, we select $\mathbb{R} = \mathrm{diag}\,(0.8, 10^{-7})$, from which

$$\mathbb{K} = \begin{bmatrix} 8.1561 & 3.1275 & 0 \\ 0 & 0 & -3161.9 \end{bmatrix} \tag{81}$$

and the closed-loop poles become

$$\lambda_{1,2} = -0.7132 \pm 0.2034\, j\,, \quad \lambda_{3,4} = -0.8864 \pm 1.8265\, j\,, \quad \lambda_5 = -29.2757\,, \quad \lambda_6 = -0.1073 \tag{82}$$

The gain matrix of Eq. (81) allow the control variables to be written as a function of the spacecraft state as

$$\delta\widetilde{\beta} = -k_{p1}\, x - k_{d1}\, v_x \tag{83}$$

$$\widetilde{\alpha} = -k_{d3}\, v_z \tag{84}$$

The non-linear dynamical equation (1) have been integrated starting from an initial perturbed state in which at time $t_0 \triangleq 0$ each position component amounts to 500 km and each velocity component amounts to 0.5 m/s, in analogy with Ref. [42]. These values are then normalized with the usual CRTBP notation, yielding

$$\boldsymbol{x}(t_0) = [\ 1.93 \qquad 1.93 \qquad 1.93 \qquad 9.60 \qquad 9.60 \qquad 9.60\ ]^{\mathrm{T}} \times 10^{-6} \tag{85}$$

The system perturbed dynamics is shown in Fig. 10, which highlights that the static output-feedback control law guarantees stability, and the spacecraft converges towards the nominal equilibrium position (i.e., the L_1-type AEP). The errors in the state vector components decrease with time, with the only exception of a first initial phase. The maximum variation of the equivalent lightness number is $\max\left|\delta\widetilde{\beta}\right| = 0.0086\,\widetilde{\beta}_e \simeq 8.62 \times 10^{-5}$, while the maximum values of $\widetilde{\alpha}$ is $\max|\widetilde{\alpha}| = 3.04\,\mathrm{deg}$, which is compatible with the previous assumption of small Euler angles.

Having defined the closed-loop system dynamics, we must calculate the maximum control torques provided by the RCDs. To that end, it is first necessary to estimate the spacecraft moments of inertia, which are obtained by assigning the reference values to the sail area, the sail density and the payload mass. As for the sail mass and density, we take the same values as that of IKAROS spacecraft, which was equipped with reflectivity control devices. In particular, IKAROS had a sail area of $196\,\mathrm{m}^2$ and a total sail loading of about $\sigma = 40\,\mathrm{g/m}^2$, including membranes and RCDs. This value should then be adjusted when the portion of RCD area has been quantified, but for the scope of a preliminary design, such an estimate is sufficiently accurate. Since IKAROS was a demonstrative mission, its mass is too large for our purposes. A more realistic mass estimate comes from the NEA Scout mission [26, 27], which is designed to carry a payload of about 14 kg.

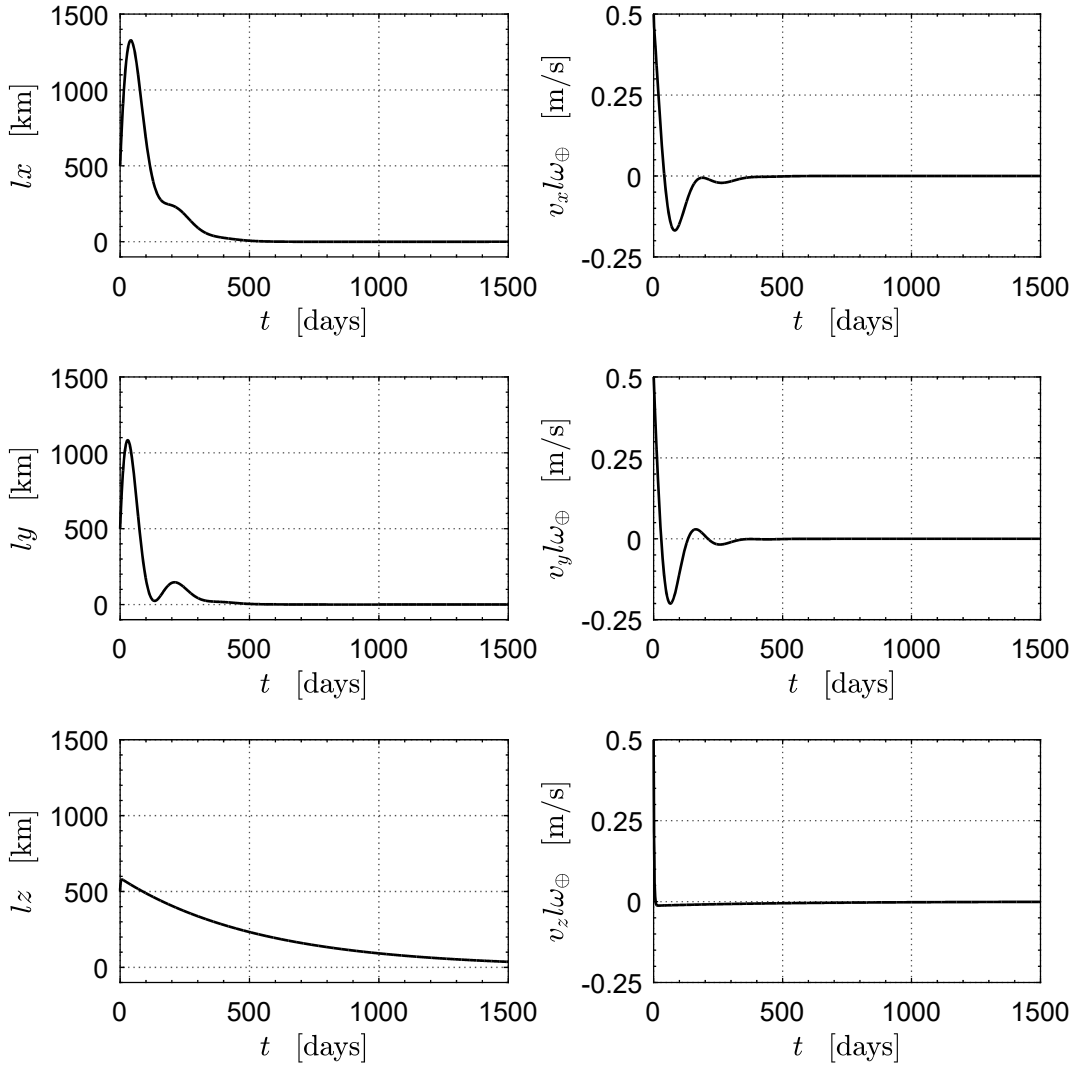

Figure 10: Time histories of state variables in the simulated test scenario when an H_∞ static output-feedback control law is applied.

The spacecraft hub is modelled as a uniform cylindrical body with a radius $R = 1\,\mathrm{m}$, a height $H = 6.5\,\mathrm{m}$, and with its axis aligned with the unit vector $\hat{\boldsymbol{n}}$. The moments of inertia may therefore be written as

$$I_1 = \frac{1}{2}(m - \sigma A)R^2 + \frac{1}{6}\sigma A^2 \simeq 260\,\mathrm{kg\,m^2} \tag{86}$$

$$I_2 = \frac{1}{12}(m - \sigma A)(3R^2 + H^2) + \frac{1}{12}\sigma A^2 \simeq 150\,\mathrm{kg\,m^2} \tag{87}$$

$$I_3 = \frac{1}{12}(m - \sigma A)(3R^2 + H^2) + \frac{1}{12}\sigma A^2 \simeq 150\,\mathrm{kg\,m^2} \tag{88}$$

Assuming those moments of inertia, the maximum required control inputs derived from Euler's equations (57)–(59) are $\max\{|M_1|, |M_2|, |M_3|\} = \{0.000, 8.1216, 0.000\} \times 10^{-6}\,\mathrm{N\,m}$. Using Eq. (75) and assuming a lever arm of 5 m, the area A_2 of each set of RCDs is equal to about $0.44\,\mathrm{m^2}$. It is now possible to complete the preliminary sizing of the solar sail by solving the algebraic system obtained by setting $\widetilde{\beta}_e = 0.0101$ in Eq. (73) and $\beta_{\max} = 0.010187$ in Eq. (74), and solving for A_s and A_1. The solution gives $A_s = 92.01\,\mathrm{m^2}$

and $A_1 = 32.65\,\mathrm{m}^2$, from which the total nominal area is $A = A_s + 2\,A_1 + 4\,A_2 = 159.07\,\mathrm{m}^2$ and the side length is about 12.61 m. Accordingly, the sail area covered by RCDs amounts to about 42% of the total.

4.1. Simplified control law

The numerical simulations show that very small torques are necessary to stabilize the motion of the solar sail-based spacecraft in the proximity of an L_1-type AEP, when the proposed control law is adopted. However, this solution has a drawback, in that the Earth-spacecraft communications are highly disturbed by the solar disk. It is therefore worth wondering whether it is possible to control the spacecraft by adjusting the lightness number $\widetilde{\beta}$ only, thus keeping the Euler's angles constant, but allowing the probe to oscillate above and below the Ecliptic to enable communications with stations on Earth, as suggested in Ref. [42]. In essence, we now assume that the equivalent normal of the wrinkled-sail is always aligned with the radial direction, that is $\widetilde{\psi} = \widetilde{\alpha} = 0$.

In this simplified version of the control system, only the gains k_{p1} and k_{d1} are taken different from zero. The new gain matrix $\mathbb{K}$ is therefore:

$$\mathbb{K} = [\ 8.1561 \quad 3.1275 \quad 0\ ] \tag{89}$$

and the closed-loop poles are

$$\lambda_{1,2} = -0.7132 \pm 0.2034\,j\,, \quad \lambda_{3,4} = -0.8864 \pm 1.8265\,j\,, \quad \lambda_{5,6} = \pm 1.7727\,j \tag{90}$$

Note that the eigenvalues corresponding to the motion along z are unaffected by the control law since in this case the z-dynamics is uncontrollable, leading to a marginally-stable motion. In this context, Fig. 11 shows the results of the system dynamics when this simplified control law is used, and highlights that the motion on the Ecliptic is asymptotically stable and practically identical to that sketched in Fig. 10. The maximum value of the equivalent lightness number is again $\max(\widetilde{\beta}) = 0.010187$.

Using this simplified control law and neglecting the orbital perturbations, the sail design does not require RCDs at its edges, that is, $A_2 = 0$. In that case, the solutions of Eqs. (73) and (74) provide $A_s = 106.42\,\mathrm{m}^2$ and $A_1 = 12.40\,\mathrm{m}^2$, and the total sail area is $A = A_s + 2\,A_1 = 131.22\,\mathrm{m}^2$, which is equivalent to a square sail with a side length of 11.5 m. The fraction of sail area covered with RCDs is about 9% only.

5. Conclusion

The generation and maintenance of an L_1-type artificial equilibrium point in the Sun-[Earth+Moon] circular restricted three-body problem has been discussed. The propulsive acceleration generated by the solar sail has been expressed with a recent thrust model, which takes into account the presence of wrinkles on the sail surface and is based on experimental measurements. Since L_1-type artificial equilibrium points are intrinsically unstable, the solar sail uses reflectivity control devices to provide the required control torques and to adjust the sail lightness number.

A proportional-derivative control strategy has been proposed to stabilize the sail dynamics, and a procedure has been proposed to provide a first estimation of the total sail area and the sail fraction covered by reflectivity control devices. Numerical simulations have shown that the controlled dynamics is stable and quickly converges to the equilibrium point. The required control torques are small and may be easily generated by reflectivity control devices, without the need of more massive actuators. A simplified control law that adjusts the wrinkled-sail lightness number has also been simulated, showing that a stable behavior can be achieved on the Ecliptic, with an oscillating dynamics along the out-of-plane direction. This feature simplifies the spacecraft communications with Earth as it avoids the scientific probe to be occulted by the solar disk.

6. Appendix: wrinkled-sail thrust model

Consider a solar sail with a total mass m, and let $\hat{\boldsymbol{n}}$ be a unit vector normal to the (nominal) sail surface in the direction opposite to the Sun. The thrust vector $\boldsymbol{T}$ may be written as a function of the Sun-spacecraft distance $l\,r_\odot$ and the sail membrane optical properties as

$$\boldsymbol{T} = \frac{P_\oplus\,A}{r_\odot^2}\,\cos\theta\left[(2\rho_s\cos\theta + \rho_d B_f + \kappa\lambda)\hat{\boldsymbol{n}} + (\kappa + \rho_d)\hat{\boldsymbol{r}}_\odot\right] \tag{91}$$

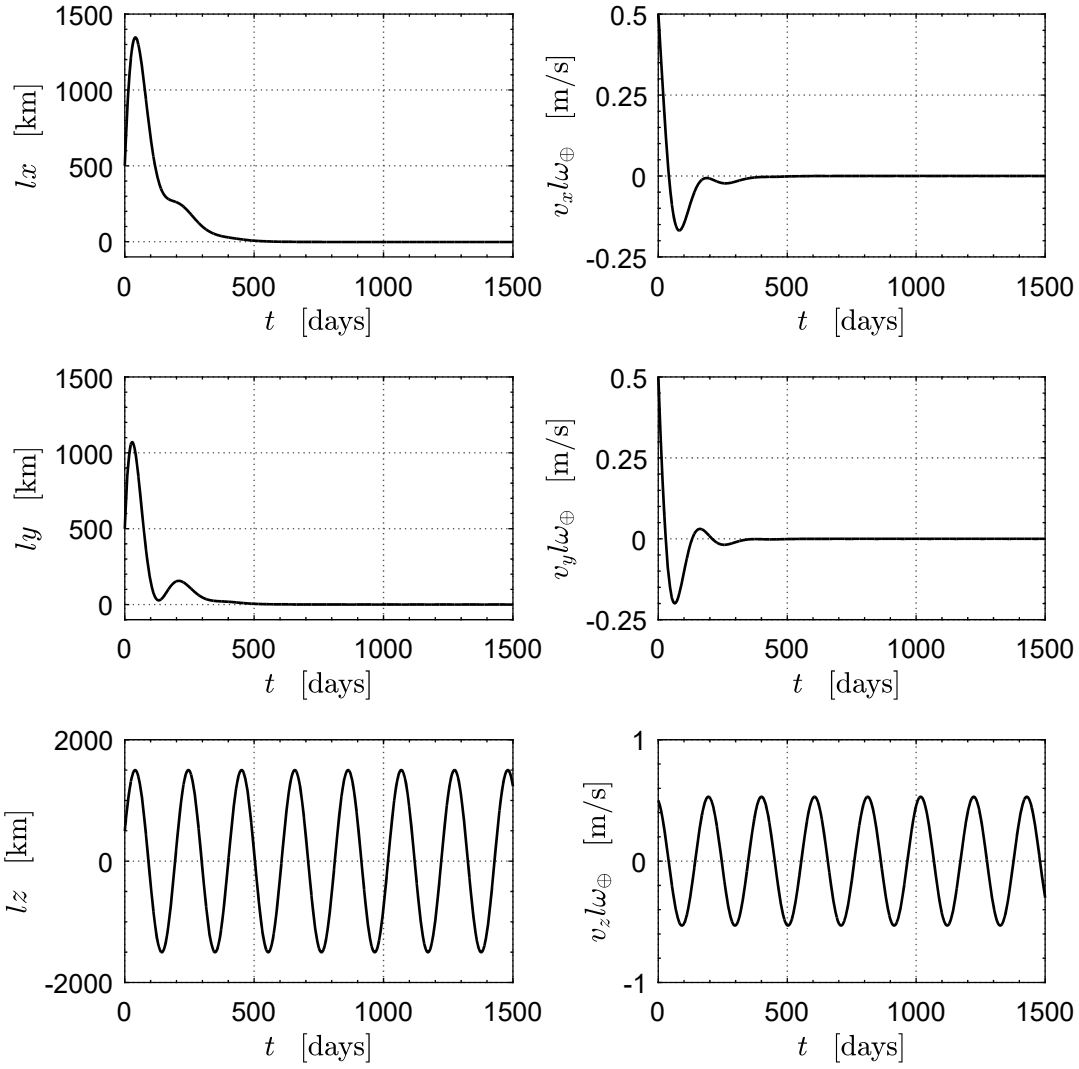

Figure 11: Time histories of state variables in the simulated test scenario when the simplified $\widetilde{\beta}$-control law is applied.

where A is the reference sail area and $\theta \in [0, \pi/2]$ rad is the sail pitch angle, that is, the angle between the directions of $\hat{\boldsymbol{r}}_\odot$ and $\hat{\boldsymbol{n}}$. The optical properties satisfy the following equation

$$\rho_s + \rho_d + \kappa = 1 \tag{92}$$

where the photon transmission through the sail membrane has been neglected. Finally, the term λ in Eq. (91) is defined as

$$\lambda \triangleq \frac{\varepsilon_f B_f - \varepsilon_b B_b}{\varepsilon_f + \varepsilon_b} \tag{93}$$

where B_f (or B_b) are the front-side (or back-side) non-Lambertian coefficients of the sail, while ε_f (or ε_b) are the front-side (or back-side) emissivity coefficients. Since the value of λ is (usually) very small, it is neglected in the rest of the analysis.

The thrust model described by Eq. (91) is valid for a (perfectly) flat solar sail. In fact, a real sail differs from a flat and perfectly-smooth surface because of several deformations that take place at different length scales. In particular, micro-scale effects, such as surface roughness of the sail material, directly affect the film optical properties and should be accounted for when determining the optical parameters, as is discussed in Ref. [58]. On the other hand, macro-scale effects, usually referred to as billowing, are deformations of the

sail shape due to the action of solar radiation pressure. These effects have been neglected in this work, but a parametric model capable of accounting for sail billowing is available in the literature [47, 61].

The most important source of deformations at an intermediate length scale are wrinkles, which are elastic responses of the sail to compressive stresses, and creases, which are inelastic deformations due to folding and handling. The effects of these deformations on the sail thrust have been evaluated in Refs. [43, 44], in terms of their magnitude and direction, and these outcomes will now be briefly summarized, along with their impact on the thrust model described by Eq. (91). Both wrinkles and creases, despite being caused by different phenomena, have the same effect on the sail reflective film and therefore no distinction will be made between these two deformations in the rest of the analysis.

When the solar sail is not (perfectly) flat due to the presence of wrinkles and creases, a single unit vector normal to the sail cannot be univocally defined. Therefore, paralleling the approach discussed by Refs. [43, 44], the sail membrane is divided into a set of small triangular elemental cells (TECs). The small dimension of each TEC allows a normal unit vector $\hat{\boldsymbol{n}}_j$ to be defined for each TEC (denoted by an index j). Accordingly, the (small) thrust contribution $\mathrm{d}\boldsymbol{T}_j$, generated by the generic j-th TEC with area $\mathrm{d}A_j$, can be written starting from Eq. (91) as

$$\mathrm{d}\boldsymbol{T}_j = \frac{P_\oplus \, \mathrm{d}A_j}{r_\odot^2} \, \cos\theta_j \Big[(2\rho_s \cos\theta_j + \rho_d B_f) \hat{\boldsymbol{n}}_j + (\kappa + \rho_d) \hat{\boldsymbol{r}}_\odot \Big] \tag{94}$$

where $\theta_j = \arccos \hat{\boldsymbol{n}}_j \cdot \hat{\boldsymbol{r}}_\odot$, and it is assumed that the optical properties are constant for each TEC in the structure.

The total thrust generated by a wrinkled solar sail is the sum of the contributions of each TEC, which may be rewritten in a more compact form by defining an equivalent normal unit vector $\widetilde{\hat{\boldsymbol{n}}}$, viz.

$$\boldsymbol{T} = \sum_{j=1}^{N_{TEC}} \mathrm{d}\boldsymbol{T}_j = \frac{P_\oplus \, A}{r_\odot^2} \, \cos\widetilde{\theta} \Big[(2\rho_s \cos\theta + \rho_d B_f) \widetilde{\hat{\boldsymbol{n}}} + (\kappa + \rho_d) \hat{\boldsymbol{r}}_\odot \Big] \tag{95}$$

where the pitch angle $\widetilde{\theta}$ is the angle between the equivalent normal $\widetilde{\hat{\boldsymbol{n}}}$ and the radial unit vector $\hat{\boldsymbol{r}}_\odot$.

When the term $\mathrm{d}\boldsymbol{T}_j$ given by Eq. (94) is substituted into Eq. (95), we obtain

$$\begin{aligned} &2\rho_s \sum_{j=1}^{N_{TEC}} \cos^2\widetilde{\theta}_j \, \hat{\boldsymbol{n}}_j \, \mathrm{d}A_j + \rho_d B_f \sum_{j=1}^{N_{TEC}} \cos\widetilde{\theta}_j \, \hat{\boldsymbol{n}}_j \, \mathrm{d}A_j + (\kappa + \rho_d) \sum_{j=1}^{N_{TEC}} \cos\widetilde{\theta}_j \, \hat{\boldsymbol{r}}_\odot \, \mathrm{d}A_j = \\ &= \Big[(2\rho_s \cos^2\Theta + \rho_d B_f \cos\Theta) \widetilde{\hat{\boldsymbol{n}}} + (\kappa + \rho_d) \cos\Theta \, \hat{\boldsymbol{r}}_\odot \Big] A \end{aligned} \tag{96}$$

which provides two independent conditions, viz.

$$\cos\Theta - \frac{1}{N_{TEC}} \sum_{j=1}^{N_{TEC}} \cos\widetilde{\theta}_j = 0 \tag{97}$$

$$\Big(2\rho_s \cos^2\Theta + \rho_d B_f \cos\Theta \Big) \widetilde{\hat{\boldsymbol{n}}} - \frac{1}{N_{TEC}} \Big(2\rho_s \sum_{j=1}^{N_{TEC}} \cos^2\widetilde{\theta}_j \hat{\boldsymbol{n}}_j + \rho_d B_f \sum_{j=1}^{N_{TEC}} \cos\widetilde{\theta}_j \hat{\boldsymbol{n}}_j \Big) = 0 \tag{98}$$

where Θ is the (small) angle between the directions of $\widetilde{\hat{\boldsymbol{n}}}$ and $\hat{\boldsymbol{n}}$.

The components of the unit vector relative to the generic j-th TEC may be written in a reference frame referred to as "sail boom frame" $\mathcal{T}_{SBF}(S; \hat{\boldsymbol{i}}_{SBF}, \hat{\boldsymbol{j}}_{SBF}, \hat{\boldsymbol{k}}_{SBF})$, see Ref. [44], the origin of which is at the center of mass S. The unit vectors $\hat{\boldsymbol{i}}_{SBF}$ and $\hat{\boldsymbol{j}}_{SBF}$ are on the sail nominal plane, aligned with the principal axes of inertia, while the third unit vector is in the opposite direction with respect to the normal of the unwrinkled sail, that is, $\hat{\boldsymbol{k}}_{SBF} = -\hat{\boldsymbol{n}}$. The components of $\hat{\boldsymbol{n}}_j$ are therefore functions of both the j-th TEC pitch angle θ_j, and of an azimuth angle ϕ_j as

$$[\hat{\boldsymbol{n}}_j]_{\mathcal{T}_{SBF}} = [-\sin\widetilde{\theta}_j \cos\widetilde{\phi}_j \quad -\sin\widetilde{\theta}_j \sin\widetilde{\phi}_j \quad -\cos\widetilde{\theta}_j \,]^{\mathrm{T}} \tag{99}$$

which allows the equivalent normal $\widetilde{\hat{\boldsymbol{n}}}$ to be expressed as a function of two equivalent spherical coordinates $\widetilde{\theta}$ and $\widetilde{\phi}$, viz.

$$[\widetilde{\hat{\boldsymbol{n}}}]_{\mathcal{T}_{SBF}} = [-\sin\widetilde{\theta}\cos\widetilde{\phi} \quad -\sin\widetilde{\theta}\sin\widetilde{\phi} \quad -\cos\widetilde{\theta}]^{\mathrm{T}} \tag{100}$$

Assume now that the $\hat{\boldsymbol{n}} \equiv \hat{\boldsymbol{r}}_{\odot}$, that is, the radial unit vector is aligned with the normal to the unwrinkled-sail. Such an arrangement is equivalent to the experimental setup of the test discussed in Ref. [44]. In this case, the angle Θ between the directions of $\hat{\boldsymbol{n}}$ and $\widetilde{\hat{\boldsymbol{n}}}$ coincides with the equivalent pitch angle $\widetilde{\theta}$ between the directions of $\widetilde{\hat{\boldsymbol{n}}}$ and $\hat{\boldsymbol{r}}_{\odot}$. Accordingly, the z-component of $\widetilde{\hat{\boldsymbol{n}}}$ may be easily obtained from Eq. (97) as

$$\widetilde{n}_z = -\cos\widetilde{\theta} = -\cos\langle\theta_j\rangle \tag{101}$$

where brackets denote the mean value calculated over all of the TECs. The other two components of $\widetilde{\hat{\boldsymbol{n}}}$ are obtained from the component along $\hat{\boldsymbol{i}}_{SBF}$ and the component along $\hat{\boldsymbol{j}}_{SBF}$ of Eq. (98) as

$$(2\rho_s\widetilde{n}_z^2 + \rho_d B_f \widetilde{n}_z)\widetilde{n}_x = 2\rho_s \ \cos^2\widetilde{\theta}_j \sin\widetilde{\theta}_j \cos\widetilde{\phi}_j + \rho_d B_f \ \langle\cos\widetilde{\theta}_j \sin\widetilde{\theta}_j \cos\widetilde{\phi}_j\rangle \tag{102}$$

$$(2\rho_s\widetilde{n}_z^2 + \rho_d B_f \widetilde{n}_z)\widetilde{n}_y = 2\rho_s \ \langle\cos^2\widetilde{\theta}_j \sin\widetilde{\theta}_j \sin\widetilde{\phi}_j\rangle + \rho_d B_f \ \langle\cos\widetilde{\theta}_j \sin\widetilde{\theta}_j \sin\widetilde{\phi}_j\rangle \tag{103}$$

According to the experimental measurements discussed in Ref [44], when $\hat{\boldsymbol{r}}_{\odot} \equiv \hat{\boldsymbol{n}}$, the following values of $\widetilde{\theta}$ and $\widetilde{\phi}$ are obtained

$$\widetilde{\theta} = 7.774\,\mathrm{deg} \tag{104}$$

$$\widetilde{\phi} = 65.81\,\mathrm{deg} \tag{105}$$

from which

$$[\widetilde{\hat{\boldsymbol{n}}}]_{\mathcal{T}_{SBF}} = [-0.055 \quad -0.123 \quad -0.991]^{\mathrm{T}} \tag{106}$$

This expression can be easily converted into the body-fixed reference frame $\mathcal{T}_B$ used in our analysis by recalling that $\hat{\boldsymbol{k}}_{SBF} \equiv -\hat{\boldsymbol{n}}$ and assuming that, without loss of generality, $\hat{\boldsymbol{i}}_{SBF} \equiv \hat{\boldsymbol{q}}$ and $\hat{\boldsymbol{j}}_{SBF} \equiv \hat{\boldsymbol{p}}$. As a result we obtain

$$[\widetilde{\hat{\boldsymbol{n}}}]_{\mathcal{T}_B} = [0.991 \quad -0.123 \quad -0.055]^{\mathrm{T}} \tag{107}$$

which coincides with Eq. (29).

Finally, the model discussed in Refs. [43, 44] also accounts for the effect of wrinkles on the total sail area. Indeed, experimental activities have shown that a solar sail sample, when loaded at its vertices, changes its perimeter due to an effect of rolling up of its edges. This affects the sail area that varies, in its turn, by an amount equal to δA_l. This effect cannot be predicted through finite-elements methods, so that experimental measures are necessary for an estimation of its magnitude. Moreover, the wrinkles reduce the total area exposed to light, and a second contribution equal to δA_w must also be accounted for. To summarize, the area variation due to the wrinkles is

$$\delta A = \delta A_l + \delta A_w \tag{108}$$

and the sail area may be rewritten as

$$\widetilde{A} = A\left(1 + \frac{\delta A}{A}\right) \tag{109}$$

The contribution between brackets in Eq. (109) is the change in magnitude of the propulsive acceleration due to the previous effect. The experimental measurements discussed in Ref. [43] show that $\delta A_l/A = -10.78\,\%$ and $\delta A_w/A = -1.82\,\%$, with a relative area variation equal to $\delta A/A = -12.60\,\%$. This implies that the thrust magnitude decreases of the same amount.

When the effects on the sail normal and on the effective area are both taken into account, the general expression for the sail thrust becomes

$$\boldsymbol{T} = \frac{P_{\oplus}\,A}{r_{\odot}^2}\left(1 + \frac{\delta A}{A}\right)\cos\widetilde{\theta}\left[(2\rho_s\cos\widetilde{\theta} + \rho_d B_f)\,\widetilde{\hat{\boldsymbol{n}}} + (\kappa + \rho_d)\,\hat{\boldsymbol{r}}_{\odot}\right] \tag{110}$$

where $\widetilde{\boldsymbol{n}}$ is given by Eq. (107), δA is provided by Eq. (108), and $\cos\widetilde{\theta} = \widetilde{\hat{\boldsymbol{n}}} \cdot \hat{\boldsymbol{r}}_{\odot}$. The expression (110) gives the dimensionless propulsive acceleration vector $\boldsymbol{a}$ of Eq. (2).

References

[1] B. Fu, E. Sperber, F. Eke, Solar sail technology - a state of the art review, Progress in Aerospace Sciences 86 (2016) 1–19, doi: 10.1016/j.paerosci.2016.07.001.

[2] S. Gong, M. Macdonald, Review on solar sail technology, Astrodynamics 3 (2) (2019) 93–125, doi: 10.1007/s42064-019-0038-x.

[3] D. A. Spencer, L. Johnson, A. C. Long, Solar sailing technology challenges, Aerospace Science and Technology 93 (2019) Article number 105276, doi: 10.1016/j.ast.2019.07.009.

[4] C. R. McInnes, Solar sail mission applications for non-Keplerian orbits, Acta Astronautica 45 (4–9) (1999) 567–575, doi: 10.1016/S0094-5765(99)00177-0.

[5] S. Gong, J. Li, Solar sail heliocentric elliptic displaced orbits, Journal of Guidance, Control and Dynamics 37 (6) (2014) 2021–2025, doi: 10.2514/1.G000660.

[6] M. Bassetto, L. Niccolai, A. A. Quarta, G. Mengali, Logarithmic spiral trajectories generated by solar sails, Celestial Mechanics and Dynamical Astronomyarticle no. 18. 130 (2), doi: 10.1007/s10569-017-9812-6.

[7] A. A. Quarta, G. Mengali, M. Bassetto, Optimal solar sail transfers to circular Earth-synchronous displaced orbits, Astrodynamics 4 (3) (2020) 193–204, doi: 10.1007/s42064-019-0057-x.

[8] L. Niccolai, A. A. Quarta, G. Mengali, Solar sail heliocentric transfers with a Q-law, Acta Astronautica 188 (2021) 352–361, doi: 10.1016/j.actaastro.2021.07.037.

[9] Y. Song, S. Gong, Solar-sail trajectory design for multiple near-Earth asteroid exploration based on deep neural networks, Aerospace Science and Technology 91 (2019) 28–40, doi: 10.1016/j.ast.2019.04.056.

[10] A. Caruso, A. A. Quarta, G. Mengali, M. Ceriotti, Shape-based approach for solar sail trajectory optimization, Aerospace Science and Technology 107, doi: 10.1016/j.ast.2020.106363.

[11] L. Niccolai, A. A. Quarta, G. Mengali, Solar sail trajectory analysis with asymptotic expansion method, Aerospace Science and Technology 69 (2017) 431–440, doi: 10.1016/j.ast.2017.05.038.

[12] X. Pan, M. Xu, R. Santos, Trajectory optimization for solar sail in cislunar navigation constellation with minimal lightness number, Aerospace Science and Technology 70 (2017) 559–567, doi: 10.1016/j.ast.2017.08.042.

[13] A. Peloni, A. V. Rao, M. Ceriotti, Automated trajectory optimizer for solar sailing (ATOSS), Aerospace Science and Technology 72 (2018) 465–475, doi: 10.1016/j.ast.2017.11.025.

[14] A. Farrés, J. Heiligers, N. Miguel, Road map to L_4/L_5 with a solar sail, Aerospace Science and Technology 95 (2019) Article number 105458, doi: 10.1016/j.ast.2019.105458.

[15] I. Dandouras, B. Pirard, J. Y. Prado, High performance solar sails for linear trajectories and heliostationary missions, Advances in Space Research 34 (1) (2004) 198–203, doi: 10.1016/j.asr.2003.02.055.

[16] A. A. Quarta, G. Mengali, L. Niccolai, Solar sail optimal transfer between heliostationary points, Journal of Guidance, Control, and Dynamics 43 (10) (2020) 1935–1942, doi: 10.2514/1.G005193.

[17] G. Mengali, A. A. Quarta, Optimal heliostationary missions of high-performance sailcraft, Acta Astronautica 60 (8-9) (2007) 676–683, doi: 10.1016/j.actaastro.2006.07.018.

[18] C. G. Sauer Jr., Solar sail trajectories for solar polar and interstellar probe missions, Advances in the Astronautical Sciences 103 (1) (2000) 1–16 .

[19] B. Dachwald, Optimal solar-sail trajectories for missions to the outer solar system, Journal of Guidance, Control, and Dynamics 28 (6) (2005) 1187–1193, doi: 10.2514/1.13301.

[20] G. Mengali, A. A. Quarta, Solar sail trajectories with piecewise-constan steering laws, Aerospace Science and Technology 13 (8) (2009) 431–441, doi: 10.1016/j.ast.2009.06.007.

[21] X. Zeng, K. T. Alfriend, J. Li, S. R. Vadali, Optimal solar sail trajectory analysis for interstellar missions, Journal of the Astronautical Sciences 59 (3) (2012) 502–516, doi: 10.1007/S40295-014-0008-y.

[22] O. Mori, Y. Shirasawa, H. Sawada, Y. Mimasu, Y. Tsuda, R. Funase, T. Saiki, T. Yamamoto, N. Motooka, Y. Kishino, J. Kawaguchi, IKAROS extended mission and advanced solar power sail mission, in: 63rd International Astronautical Congress (IAC), Naples, Italy, 2012.

[23] L. Johnson, M. Whorton, A. Heaton, R. Pinson, G. Laue, C. Adams, NanoSail-D: A solar sail demonstration mission, Acta Astronautica 68 (5–6) (2011) 571–575, doi: 10.1016/j.actaastro.2010.02.008.

[24] D. A. Spencer, B. Betts, J. M. Bellardo, A. Diaz, B. Plante, J. R. Mansell, The LightSail 2 solar sailing technology demonstration, Advances in Space Research 67 (9) (2021) 2878–2889, doi: 10.1016/j.asr.2020.06.029.

[25] O. Mori, J. Matsumoto, T. Chujo, M. Matsushita, H. Kato, T. Saiki, Y. Tsuda, J. Kawaguchi, F. Terui, Y. Mimasu, G. Ono, N. Ogawa, Y. Takao, Y. Kubo, K. Ohashi, A. K. Sugihara, T. Okada, T. Iwata, H. Yano, Solar power sail mission ok OKEANOS, Astrodynamics 4 (3) (2020) 233–248, doi: 10.1007/s42064-019-0067-8.

[26] L. McNutt, L. Johnson, P. Kahn, J. Castillo-Rogez, A. Frick, Near-earth asteroid (NEA) scout, in: AIAA SPACE 2014 Conference and Exposition, San Diego (CA), USA, 2014, paper AIAA 2014-4435.

[27] J. B. Pezent, R. Sood, A. Heaton, High-fidelity contingency trajectory design and analysis for NASA's near-earth asteroid (NEA) Scout solar sail Mission, Acta Astronautica 159 (2019) 385–396, doi: 10.1016/j.actaastro.2019.03.050.

[28] T. R. Lockett, J. Castillo-Rogez, L. Johnson, J. Matus, J. Lightholder, A. Marinan, A. Few, Near-Earth Asteroid Scout Flight Mission, IEEE Aerospace and Electronic Systems Magazine 35 (3) (2020) 20–29, doi: 10.1109/MAES.2019.2958729.

[29] J. B. Pezent, R. Sood, A. Heaton, K. Miller, L. Johnson, Preliminary trajectory design for NASA's Solar Cruiser: A technology demonstration mission, Acta Astronautica 183 (2021) 134–140, doi: 10.1016/j.actaastro.2021.03.006.

[30] W. S. Koon, M. W. Lo, J. E. Marsden, S. D. Ross, Dynamical systems, the three-body problem and space mission design, Marsden Books, 2011.

[31] H. H. Selim, J. L. G. Guirao, E. I. Abouelmagd, Libration points in the restricted three-body problem: Euler angles, existence and stability, Discrete and Continuous Dynamical Systems - Series S 12 (45) (2019) 703–710, doi: 10.3934/dcdss.2019044.

[32] E. I. Abouelmagd, A. A. Ansari, The motion properties of the infinitesimal body in the framework of bicircular Sun perturbed Earth–Moon system, New Astronomy 73, doi: 10.1016/j.newast.2019.101282.
[33] G. Aliasi, G. Mengali, A. A. Quarta, Artificial equilibrium points for a generalized sail in the circular restricted three-body problem, Celestial Mechanics and Dynamical Astronomy 110 (4) (2011) 343–368, doi: 10.1007/s10569-011-9366-y.
[34] A. Farrés, A. Jorba, Artificial equilibria in the RTBP for a solar sail and applications, Astrophysics and Space Science Proceedings 44 (2016) 73–89, doi: 10.1007/978-3-319-23986-6_6.
[35] F. J. T. Salazar, C. R. McInnes, O. C. Winter, Periodic orbits for space-based reflectors in the circular restricted three-body problem, Celestial Mechanics and Dynamical Astronomy 128 (1) (2017) 95–113, doi: 10.1007/s10569-016-9739-3.
[36] E. C. Stone, A. M. Frandsen, R. A. Mewaldt, E. R. Christian, D. Margolies, J. F. Ormes, F. Snow, The Advanced Composition Explorer, Space Science Reviews 86 (1–4) (1998) 1–22, doi: 10.1023/A:1005082526237.
[37] Y. Tsuda, O. Mori, R. Funase, H. Sawada, T. Yamamoto, T. Saiki, T. Endo, J. Kawaguchi, Flight status of IKAROS deep space solar sail demonstrator, Acta Astronautica 69 (9–10) (2011) 833–840, doi: 10.1016/j.actaastro.2011.06.005.
[38] R. Funase, Y. Shirasawa, Y. Mimasu, O. Mori, Y. Tsuda, T. Saiki, J. Kawaguchi, On-orbit verification of fuel-free attitude control system for spinning solar sail utilizing solar radiation pressure, Advances in Space Research 48 (11) (2011) 1740–1746, doi: 10.1016/j.asr.2011.02.022.
[39] G. Aliasi, G. Mengali, A. A. Quarta, Artificial equilibrium points for a generalized sail in the elliptic restricted three-body problem, Celestial Mechanics and Dynamical Astronomy 114 (1-2) (2012) 181–200, doi: 10.1007/s10569-012-9425-z.
[40] G. Aliasi, G. Mengali, A. A. Quarta, Artificial Lagrange points for solar sail with electrochromic material panels, Journal of Guidance, Control and Dynamics 36 (5) (2013) 1544–1550, doi: 10.2514/1.58167.
[41] L. Niccolai, A. Caruso, A. A. Quarta, G. Mengali, Artificial collinear Lagrangian point maintenance with electric solar wind sail, IEEE Transactions on Aerospace and Electronic Systems 56 (6) (2020) 4467–4477, doi: 10.1109/TAES.2020.2990805.
[42] L. Niccolai, G. Mengali, A. A. Quarta, A. Caruso, Feedback control law of solar sail with variable surface reflectivity at Sun-Earth collinear equilibrium points, Aerospace Science and Technology 106, doi: 10.1016/j.ast.2020.106144.
[43] T. Pino, C. Circi, G. Vulpetti, Wrinkling analysis for small solar-photon sails: An experimental and analytic approach for trajectory design, Advances in Space Research 63 (11) (2019) 3675–3690, doi: 10.1016/j.asr.2019.02.016.
[44] G. Vulpetti, D. Apponi, X. Zeng, C. Circi, Wrinkling analysis of solar-photon sails, Advances in Space Research 67 (9) (2021) 2669–2687, doi: 10.1016/j.asr.2020.07.016.
[45] J. Gadewadikar, F. L. Lewis, M. Abu-Khalaf, Necessary and sufficient conditions for H_∞ static output-feedback control, Journal of Guidance, Control, and Dynamics 29 (4) (2006) 915–920, doi: 10.2514/1.16794.
[46] J. L. Wright, Space Sailing, Gordon and Breach Science Publishers, 1992, pp. 223–233, ISBN: 978-2881248429.
[47] C. R. McInnes, Solar Sailing: Technology, Dynamics and Mission Applications, Springer-Praxis Series in Space Science and Technology, Springer-Verlag, Berlin, Germany, 1999, pp. 46–54.
[48] B. Dachwald, W. Seboldt, M. Macdonald, G. Mengali, A. A. Quarta, C. R. McInnes, L. Rios-Reyes, D. J. Scheeres, B. Wie, M. Görlich, F. Lura, B. Diedrich, V. Baturkin, V. L. Coverstone, M. Leipold, G. P. Garbe, Potential solar sail degradation effects on trajectory and attitude control, in: AIAA Guidance, Navigation, and Control Conference and Exhibit, San Francisco (CA), USA, 2005, paper AIAA 2005-6172.
[49] B. Dachwald, M. Macdonald, C. R. McInnes, G. Mengali, A. A. Quarta, Impact of optical degradation on solar sail mission performance, Journal of Spacecraft and Rockets 44 (4) (2007) 740–749, doi: 10.2514/1.21432.
[50] B. Fu, F. Eke, Further investigation of the body torques on a square solar sail due to the displacement of the sail attachment points, Aerospace Science and Technology 50 (2016) 281–294, doi: 10.1016/j.ast.2016.01.007.
[51] X. Hu, S. Gong, Flexibility influence on passive stability of a spinning solar sail, Aerospace Science and Technology 58 (2016) 60–70, doi: 10.1016/j.ast.2016.08.005.
[52] B. Fu, R. T. Farouki, F. O. Eke, Equilibrium configuration of a bounded inextensible membrane subject to solar radiation pressure, Aerospace Science and Technology 68 (2017) 552–560, doi: 10.1016/j.ast.2017.06.018.
[53] S. Firuzi, S. Gong, Refractive sail and its applications in solar sailing, Aerospace Science and Technology 77 (2018) 362–372, doi: 10.1016/j.ast.2018.03.016.
[54] M. Bassetto, A. A. Quarta, G. Mengali, V. Cipolla, Trajectory analysis of a sun-facing solar sail with optical degradation, Journal of Guidance, Control, and Dynamics 43 (9) (2020) 1727–1732, doi: 10.2514/1.G005214.
[55] G. Mengali, A. A. Quarta, Optimal three-dimensional interplanetary rendezvous using nonideal solar sail, Journal of Guidance, Control, and Dynamics 28 (1) (2005) 173–177, doi: 10.2514/1.8325.
[56] L. Niccolai, A. A. Quarta, G. Mengali, Analytical solution of the optimal steering law for non-ideal solar sail, Aerospace Science and Technology 62 (2017) 11–18, doi: 10.1016/j.ast.2016.11.031.
[57] A. F. Heaton, A. B. Artusio-Glimpse, An update to NASA reference solar sail thrust model, in: AIAA SPACE 2015 Conference and Exposition, Pasadena (CA), USA, 2015, paper AIAA 2015-4506.
[58] A. Heaton, N. Ahmad, K. Miller, Near earth asteroid scout thrust and torque model, in: The 4th International Symposium on Solar Sailing, no. 17055, Kyoto, Japan, 17–20 January, 2017.
[59] R. M. Young, Updated heliostorm warning mission: enhancements based on new technology, in: 48th AIAA/ASME/ASCE/AHS/ASC Structures, Structural Dynamics, and Materials Conference, Honolulu (HI), USA, 2007.
[60] S. N. Adeli, V. Lappas, B. Wie, A scalable bus-based attitude control system for solar sails, Advances in Space Research 48 (11) (2011) 1836–1847, doi: 10.1016/j.asr.2011.08.024.
[61] G. Mengali, A. A. Quarta, Optimal control laws for axially symmetric solar sails, Journal of Spacecraft and Rockets 42 (6) (2005) 1130–1133, doi: 10.2514/1.17102.